Spring 2009

Growth and Characterization of Chromium Doped Indium Oxide Diluted Magnetic Semiconductors

Ndubuisi Benjamin Ukah

GROWTH AND CHARACTERIZATION OF CHROMIUM DOPED INDIUM OXIDE DILUTED MAGNETIC SEMICONDUCTORS

A Masters Thesis

Presented to

The Graduate College of

Missouri State University

In Partial Fulfillment

Of the Requirements for the Degree

Master of Science, Materials Science

By

Ndubuisi Benjamin Ukah

May 2009

GROWTH AND CHARACTERIZATION OF CHROMIUM DOPED INDIUM OXIDE DILUTED MAGNETIC SEMICONDUCTORS

Physics, Astronomy, and Material Science

Missouri State University, May 2009

Master of Science

Ndubuisi Benjamin Ukah

ABSTRACT

Recently, enormous research efforts have been directed at diluted magnetic semiconductors (DMS) critical for realization of multi-functional spintronic devices. However, the origin of electronic and magnetic properties in DMS is not well understood. This study is aimed to better understand the structural, optical, magnetic, and magneto-transport property relationships of Cr-doped In_2O_3 (In_2O_3:Cr) DMS grown under different partial oxygen pressures on sapphire substrates using pulsed laser deposition technique. The thin films were characterized using various state-of-the-art techniques such as x-ray diffraction (XRD), UV-VIS spectroscopy, magnetotransport, and SQUID magnetometer. Expansions in lattice parameter (10.10 Å to 10.34 Å) and crystal size (13.9 nm to 35.5 nm) in these films with an increase in oxygen growth pressure as observed from XRD analysis are traceable to the reduction in oxygen vacancies (OVA). Optical analysis showed a redshift in absorption edges of the samples from 3.93 eV to 3.76 eV with an increase in oxygen growth pressure, which is attributed to the significant improvement in crystallinity. Magnetotransport results revealed that films grown at low oxygen pressures (high OVA) exhibited semiconductor-to-metallic transitions while film grown at high oxygen pressure (low OVA) showed typical semiconductor behavior. The films exhibited paramagnetism/antiferromagnetism as observed from magnetization data collected using a SQUID magnetometer. The observed magnetic behavior is possibly due to Cr clustering. This investigation reveals the important role of oxygen vacancies in the structural and electro-magneto-optical properties of In_2O_3:Cr DMS. Understanding of DMS is critical for the realization of spintronic devices such as spin field effect transistors.

KEYWORDS: semiconductors, transparent conducting oxide, pulsed laser deposition, indium oxide, opto-electronic properties

This abstract is approved as to form and content

_____

Dr. Kartik Ghosh
Chairperson, Advisory Committee
Missouri State University

GROWTH AND CHARACTERIZATION OF CHROMIUM DOPED INDIUM OXIDE DILUTED MAGNETIC SEMICONDUCTORS

By

Ndubuisi Benjamin Ukah

A Masters Thesis
Submitted to the Graduate College
Of Missouri State University
In Partial Fulfillment of the Requirements
For the Degree of Master of Science, Materials Science

May 2009

Approved:

_____
Dr. Kartik Ghosh

_____
Dr. Pawan Kahol

_____
Dr. Bryan Breyfogle

_____
Frank Einhellig, Graduate College Dean

ACKNOWLEDGEMENTS

I would like to express my sincere gratitude to my supervisor, Dr. Kartik Ghosh for affording me the opportunity to work with him. I am also thankful to the Department Head, Dr. Pawan Kahol and Dr. Bryan Breyfogle for their invaluable advice and guidance towards the successful completion of this research work. I would like to give special thanks to Dr. Kandiah Manivannan for his critical reading and comments of this thesis.

May I express my indebtedness and gratitude to my loving parents, sister and brothers for their support, encouragement, sacrifice, and prayers throughout the duration of the program. I pray for the blessings of Almighty God on them.

I am sincerely grateful to Dr. Ram Gupta, who stood by me every step of the way, and was ever ready to discuss and direct at all times. I would also like to thank Dr. Ryan Giedd and his staff members at JVIC for availing me the opportunity of a summer internship as well as their characterization equipment. Also appreciated are the support and prayers of friends and well-wishers especially Mr. & Mrs. Tom Carter.

TABLE OF CONTENTS

LIST OF TABLES

Table **Page**

LIST OF FIGURES

Figure **Page**

CHAPTER 1

INTRODUCTION

Until recently, semiconductor research has been restricted to the conventional semiconductor electronics, which is based only on the manipulation of the charge of the electron leaving out the spin. Owing to the realization of the need to manipulate both the spin and the charge of the electron arising from its relevance to spin electronics, intense research efforts have been directed at realizing ferromagnetic semiconductor materials with Curie temperatures (T_C) especially above room temperature.[1,2] Spin electronics or spintronics is a relatively new research field, and as the name implies, is a form of technology that utilizes both the spin and charge of the electron and have possible applications in spin transistors, spin-polarized solar cells, and magnetic random access memories etc. The spin of an electron is shown as a detectable weak magnetic energy state characterized by a "spin-up'' or a "spin-down''. This implies that one necessarily needs systems that can generate as well as detect currents of spin-polarized electrons so as to be able to realize a spintronic device. It is believed that magnetic semiconductors could lead to seamless electrical manipulation of magnetic states and magnetic modification of electrical signals, which could result in the realization of such devices as magnetic bipolar transistors that are able to transfer information from magnetic media to conventional semiconductor circuits. It turns out that a fundamental step towards harnessing the full potentials of spintronics lies in finding semiconducting materials with electrically tunable ferromagnetism above room temperature which can be incorporated into complex circuits. Some of the conventional semiconductor materials that are of importance to magnetic semiconductor research include GaN, GaAs, ZnO, In_2O_3, TiO_2.

Transition metals such as Fe, Mn, Co, Cr, and Ni are also important in spintronics.

1.1 Diluted magnetic semiconductors (DMS)

Diluted magnetic semiconductors (DMS) are promising materials for spintronic applications. DMS are formed when transition metals such as Fe, Co or Mn are doped into a semiconductor host lattice such as GaN or TiO_2. The research field of DMS got a boost with the theoretical prediction of room temperature ferromagnetism in Mn-doped ZnO and SnO_2 coupled with the discovery of ferromagnetism in Mn-doped InAs and GaAs; although, at Curie temperatures less than room temperature.[3,4] The presence of these transition metal ions in these semiconductors results in an indirect exchange interaction between their localized d electron spins and the itinerant conduction electrons or holes of the semiconductors giving rise to interesting magnetic field induced functionalities such as hysteresis and anomalous Hall effect, which are important for spintronic device applications.

1.2 Oxide-based DMS

The need to develop next generation multifunctional spintronic devices necessitates the search for semiconducting oxides with tunable charge carrier density, high carrier mobility, and high optical transparency. The initial reports of ferromagnetic ordering in oxides were for Co-doped TiO_2 (anatase), ZnO, and SnO_2.[5,6,7,8] Generally, existence of inherent oxygen vacancies in oxides makes them n-type conducting and attractive for magneto-optoelectronic applications. Various demonstrations of room temperature ferromagnetism have been reported for Mn-doped ZnO,[9] Ni-doped ZnO,[10] and Co-doped ZnO.[11] TiO_2 is a considerably well researched DMS material and has been reported to exhibit room temperature ferromagnetism when doped with transition metals.

Room temperature ferromagnetic ordering has been shown for Fe-doped TiO_2,[12] Ni-doped TiO_2,[13] and Co-doped TiO_2[14] systems. Co-doped SnO_2 has been reported to exhibit high Curie temperature and high saturation magnetization (Ms = 7.5μ_B/Co ion).[15] Room temperature ferromagnetism has also been demonstrated in Mn- and Fe-doped SnO_2.[16,17] Recently, magnetic doped In_2O_3 has been shown to have superior optical as well as DMS properties.

1.3. Cr-doped In_2O_3 DMS

Recently, various demonstrations of room temperature ferromagnetism such as Ni-doped In_2O_3 have been reported[18]. J. Philip et al.[19] have reported high temperature ferromagnetism in Cr-doped In_2O_3 thin films grown by co-evaporation technique, and proposed that carrier-mediation is responsible for the observed magnetic behavior. According to their report, the electrical and magnetic behavior of Cr-doped In_2O_3 – ranging from ferromagnetic metal-like (n_c = 3 x 10^{20} cm^{-3}, M_s = 1.5 μ_B/Cr) to ferromagnetic semiconducting (n_c = 1 x 10^{20}, M_s = 1.25 μ_B/Cr) to paramagnetic insulating (n_c = 9 x 10^{18} cm^{-3}) can be controllably tuned by varying the defect concentration (oxygen vacancies) in these films. It must be pointed out that an exact theoretical explanation for the origin of ferromagnetism in DMS is still unclear. P. Kharel et al.[20] have also reported the demonstration of room temperature ferromagnetism in spin-coated Cr-doped In_2O_3 thin films and bulk samples only after high vacuum annealing of the samples. The carrier densities and saturation magnetization values for the thin film and bulk samples are 6.6 x 10^{17} cm^{-3} (0.22 μ_B/Cr) and 7 x 10^{18} cm^{-3} (0.008 μ_B/Cr) respectively. Average optical transparency values of ~ 88 % and ~ 80 % have been reported for Ti-doped In_2O_3 and Zn-doped In_2O_3 thin films respectively.[21,22] This suggests

that electrical, optical as well as magnetic properties of indium oxide thin films are dependent on the growth technique. However, there is no report available on Cr-doped In_2O_3 DMS grown using PLD.

1.4 Objective

This work is on oxide-based DMS with special focus on chromium doped indium oxide. As earlier mentioned, ferromagnetic ordering in DMS is believed to be brought about by a mediation of the itinerant host semiconductor carriers between the localized electron spins of the transition metal dopant. Because of the inherent oxygen vacancies in In_2O_3 which give rise to n-type conductivity, it turns out that film growth parameters such as oxygen pressure in the growth chamber and growth temperature etc, can be effectively used to tune the oxygen vacancies thereby tuning the carrier concentration. We aim to understand the structural, optical, electrical, magnetic, and magneto-transport property relationships of In_2O_3:Cr thin films grown under different partial oxygen pressures using pulsed laser deposition.

This thesis is basically presented in five chapters, starting with an introduction followed by summarized statements about previous work on DMS, especially transparent oxide-based DMS. Chapter two discusses theory of semiconductors, charge transport mechanisms, and ferromagnetism in oxide-based DMS. In chapter three, film growth, various characterization techniques, and fabrication of samples are briefly outlined. In chapter four, experimental results are discussed in details. The report ends with some conclusions in chapter five.

CHAPTER 2

THEORY

2.1. Semiconductors

As the name implies, semiconductors are a group of materials with conductivity that lie between metals and insulators, and whose conductivity can be tuned over orders of magnitude by changes in temperature, optical excitation, and impurities. Semiconductors composed of single species of atoms found in column IV of the periodic table are referred to as elemental semiconductors. Semiconductors made up of compounds of column III and V atoms as well as column II and VI atoms are referred to as compound semiconductors. There are also oxide semiconductors. Table 2.1 below contains a list of some common semiconductors.

Table 2.1. Some common semiconductors

Group IV Semiconductors	III-V Semiconductors	II-VI Semiconductors	Oxide Semiconductors
Si	GaN	ZnS	In_2O_3
Ge	GaAs	CdSe	ZnO

It turns out that semiconductors at 0 K have a filled valence band separated from an empty conduction band by a band gap containing no allowed energy states - the same as insulators. The difference lies in the size of the band gap, which is smaller in semiconductors than in insulators. The relatively small band gap of these semiconductors enables the excitation of electrons from the valence band to the conduction band by

reasonable amounts of optical or thermal energy resulting in electrical conductivity. For instance, at room temperature, a semiconductor (Si) with a band gap of 1.1 eV will have a significant number of electrons excited thermally across the energy gap into the conduction band, whereas an insulator (SiO_2) with a band gap of ~ 9.0 eV will have a negligible number of excitations. A fundamental difference between semiconductors and insulators is that the number of electrons available for electrical conduction can be increased significantly in semiconductors by thermal or optical energy. Also conductivity in pure semiconductors can be engendered by an introduction of a limited amount of an impurity atom (doping) to the semiconductor host lattice. For example, an introduction of a limited quantity of arsenic, phosphorus or boron to silicon results in the creation of mobile electrons or holes, and this gives rise to electrical conductivity in silicon.

2.2 Direct and indirect band gap semiconductors

Energy band gap (E_g) is defined as the energy separation between the highest valence band maximum and the lowest conduction band minimum. There are two types of semiconductors based on the type of band gap: direct band gap semiconductors and indirect band gap semiconductors. A close examination of Figs. 2.1 (a) and (b) reveals some important facts about semiconductors with direct and indirect band gap. The major difference between direct and indirect band gap semiconductors is the location of the lowest conduction band minima in relation to the highest valence band maxima. For the direct band, both the highest valence band maximum and the lowest conduction band minimum occur at the same point in K-space. This feature has enormous consequences on optical processes such as electronic transitions between the valence and conduction bands. For the indirect band gap semiconductor, the highest valence band maximum and

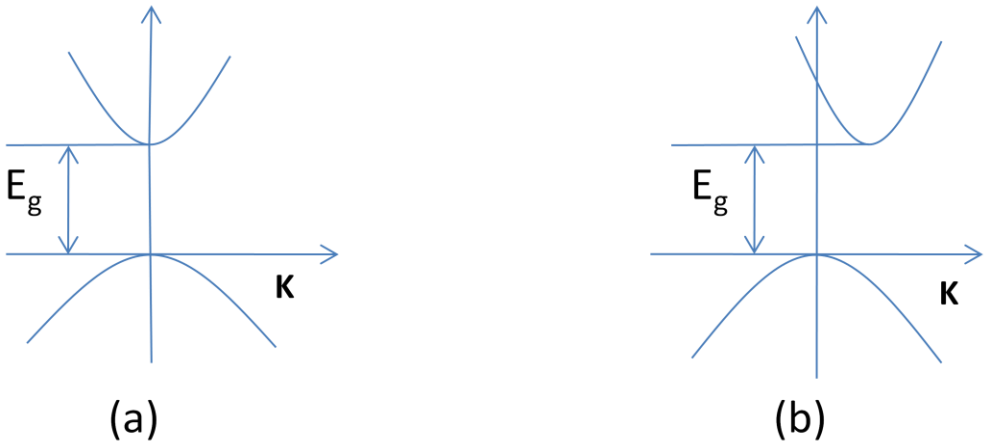

Figure 2.1. Schematic diagrams of the band structures of (a) direct band gap and (b) indirect band gap semiconductors.

the lowest conduction band minimum occur at different points in k-space. This also is of great importance in optical processes.

2.3 Extrinsic semiconductors

An intrinsic (pure) semiconductor is a perfect semiconductor crystal with no lattice defects or impurities. In these materials, there are no charge carriers at 0 K because of the completely filled valence band and completely empty conduction band, while at higher temperatures, electron-hole pairs are generated due to the thermal excitation of valence band electrons across the band gap into the conduction band. Since the charge carriers in intrinsic semiconductors are generated by thermal/optical excitation, the concentration of electrons in the conduction band is always equal to the concentration of holes in the valence band. Besides the intrinsic carriers generated thermally, it is possible to create carriers in semiconductors and consequently vary the semiconductor conductivity by intentionally introducing impurities into the crystal via a process called doping. An extrinsic semiconductor is obtained when a semiconductor crystal is doped

such that the equilibrium electron concentration differs from the equilibrium hole concentration by larger amount. By doping, a crystal can be altered so that it can have a prevalence of either electrons or holes, which leads to the existence of two types of doped semiconductors – n-type (mostly electrons) and p-type (mostly holes). The introduction of impurities or lattice defects in a perfect crystal creates additional energy levels in the band structure usually within the band gap. For instance, introduction of a column V impurity atom such as As or P (donor impurity) to Si or Ge creates an energy level filled with electrons at 0 K just at the edge of the conduction band, and as a result, only a small amount of energy is required to excite these electrons to the conduction band. Thus with a slight increase in temperature nearly all electrons at the impurity (donor) level are excited to the conduction band. This type of semiconductor is referred to as n-type since the electron concentration is far greater than the hole concentration due to the donor doping. In the same way, introduction of a column III impurity atom such as B, Al or Ga to Si or Ge results in the creation of an energy level empty of electrons at 0 K, just at the valence band edge. At low temperatures, enough thermal energy is available to excite electrons from the valance band to the impurity (acceptor) level leaving behind holes in the valence band. This type of semiconductor is referred to as p-type since the hole concentration is far greater than the electron concentration as a result of the acceptor doping.

2.4 Charge transport in semiconductors

Because of the exhibition of negative temperature coefficient of resistivity (TCR) by different transport mechanisms coupled with the complex nature of temperature dependent electrical transport in semiconductors, theoretical explanation and modeling have remained difficult. Various transport models have been proposed for disordered

systems in either the metallic regime or the Anderson-localization regime.[23,24] It also turns out that all transport models for systems in the Anderson-localization regime involve phonon-assisted hopping (or tunneling) models and the variable-range hopping (VRH) model. The models can be expressed using the relation[25]

$$\rho(T) = B_1 \exp\left[\left(\frac{B_2}{t}\right)^{1/p}\right] \tag{2.1}$$

where, B_1, B_2, and p are constants. A conduction mechanism dominated by hopping between localized states distributed randomly in the film – 3D variable-range hopping (VRH) is represented by Eq. (2.1) with $p = 4$. Another hopping conduction mechanism – nearest neighbor hopping (NNH) characterized by $p = 1$, is used to describe a system dominated by hopping between localized states distributed in a periodic array. Variable-range hopping in a coulomb gap or in a system characterized by a distribution of small metallic grains separated by thin insulating layers – granular-metal system, could be represented by $p = 2$. In such systems, the charging energy, E_C varies inversely with the capacitance, C as shown by the relation,

$$E_C = \frac{\eta e^2}{2C} \tag{2.2}$$

where η is a constant and e is the electronic charge. The charging energy governs the resistance. However, there exists a variety of other disordered systems, in which most of the conduction electrons are delocalized and are free to move over distances very large as compared to the atomic dimensions. For these random systems, the electrical conduction is dominated by electron transfer between large conducting segments separated by small

insulating barriers (fluctuation induced tunneling) rather than by hopping between localized states, and $\rho(T)$ is given by[26]

$$\rho(T) = B_3 \exp\left(\frac{t_1}{t + t_0}\right) \tag{2.3}$$

where B_3 is a constant and t_0 and t_1 are related to the properties of the insulating barriers between the metallic clusters and obtained from the relation[26]

$$t_0 = \frac{16\varepsilon_0 \hbar A V_0^{3/2}}{\pi (2m)^{1/2} w^2 e^2 K_B} \tag{2.4}$$

and

$$t_1 = \frac{8\varepsilon_0 A V_0^2}{e^2 K_B w} \tag{2.5}$$

where A is the barrier area, V_0 is the barrier height, m is the charge carrier mass, w is the barrier width, ε_0 is the permittivity of free space, and $\hbar$ is Planck's constant divided by 2π. For degenerately doped semiconductors, ionized impurity scattering has been observed to be responsible for negative temperature coefficient of resistivity, and is given by the relation

$$\rho(T) \alpha\ t^{-3/2} \tag{2.6}$$

2.5 Ferromagnetism and magnetic materials

Magnetism is a phenomenon by which materials assert attractive or repulsive influences on other materials. Iron remains the most well-known magnetic material; however, all substances are influenced to some degree by the presence of a magnetic field. The magnetic moment of an electron has three principal sources: (a) the spin of the electron, (b) the orbital angular momentum about a nucleus, (c) the change in the orbital moment

caused by an applied magnetic field. Effects (a) and (b) give paramagnetic contribution to the magnetization and (c) gives a diamagnetic contribution. The spin and orbital moments for atoms with filled electron shells are zero, and unfilled shells have finite moments. The magnetic moment per unit volume is referred to as magnetization, M, and the magnetic susceptibility χ is given by

$$\chi = \frac{M}{B} \tag{2.7}$$

where B is the macroscopic magnetic field intensity. Examples of materials which exhibit ferromagnetism – the magnetic phenomenon of interest in this work are: iron, cobalt, nickel, and gadolinium.

A ferromagnet possesses a magnetic moment even in the absence of an applied magnetic field, and manifests large and permanent magnetizations. The presence of spontaneous moment indicates that electron spins and magnetic moments are arranged in a regular fashion – uncancelled electron spins as a consequence of the electron structure. In a ferromagnet, net spin magnetic moments of adjacent atoms align with one another over relatively large volume of the crystal even in zero external field as a result of coupling interactions. The origin of these coupling forces, though still unclear, is believed to be due to the electronic structure of the metal. The saturation magnetization, M_S of a ferromagnet results when all magnetic dipoles in a solid material are mutually aligned in the direction of the external field. In the mean-field approximation, it is assumed that each magnetic atom experiences a field proportional to the magnetization as given by the relation

$$B_E = \lambda M \tag{2.8}$$

where λ is a constant independent of temperature. The Curie temperature T_C is the temperature above which the spontaneous magnetization varnishes. For $T > T_C$, the materials is in the paramagnetic phase, and for $T < T_C$ it is in the ordered ferromagnetic state as shown in figure 2.2.

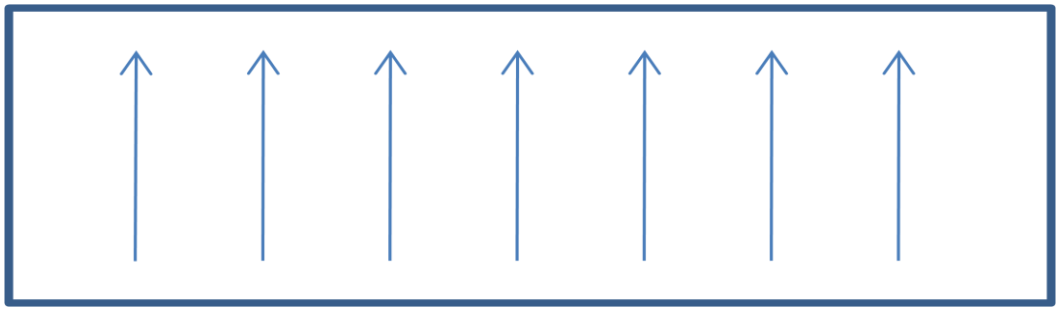

Figure 2.2. Schematic diagram of a simple ferromagnet

2.6 Ferromagnetism in oxide semiconductors

It turns out that despite considerable research efforts made in the field of DMS, exact theoretical explanation for the observation of ferromagnetic ordering in these materials is still elusive; although, there exists some theoretical models aimed at explaining ferromagnetism in both the III-V and oxide transition metal doped semiconductors.

The Zener ferromagnetic double exchange model predicts that ferromagnetism arises from exchange coupling between local moments and band electrons. It assumes that ferromagnetism is mediated by shallow acceptors in a matrix of localized spins in diluted magnetic semiconductors (DMS)[27]. It was used to explain earlier observations of ferromagnetism in (Ga,Mn)As,[28] where it assumes that the transition energy from Mn^{3+} to

Mn^{2+} lies well below the top of the valence band and that the transition energy from Mn^{2+} to Mn^{+} lies well above the bottom of the conduction band.

The donor impurity band exchange model put forward by Coey et al.[29] is based on the premise that conventional super-exchange or double exchange cannot give rise to long-range magnetic order at such small concentrations of cations obtainable in DMS experiments. This model predicts that ferromagnetic exchange in nitrides and oxides is due to mediation by shallow donor electrons that form bound magnetic polarons, which overlap to create a spin-split impurity band. It also predicts a phase diagram for an oxide semiconductor as a function of doping and carrier concentration as well as a general oxide formula given by

$$(A_{1-x}B_x)(O\square_{\delta})_n \qquad (2.18)$$

where, A is the non-magnetic ion, B is the dopant ion and $\square$ denotes the donor defects. The donor polaron and cation percolation thresholds δ_p and x_p respectively determine the occurrence of different magnetic phases. This model predicts that in oxides, ferromagnetism occurs when $\delta > \delta_p$ and $x < x_p$, while antiferromagnetism or ferimagnetism is obtained when $x > x_p$. The complex magnetic phase diagram for oxide-based DMS is shown in Fig. 2.3. The RKKY exchange model is usually employed to explain ferromagnetism in systems where the Fermi level lies below the mobility edge and the separation of magnetic cation neighbors is less than the localization length[30]. It is usually used to predict magnetic order at high donor concentrations, where the impurity-band exchange model breaks down, and the donor states merge with the bottom of the conduction band. The RKKY interaction is always ferromagnetic at low electron densities since the wave vector K_F is small at the bottom of the band, while it is

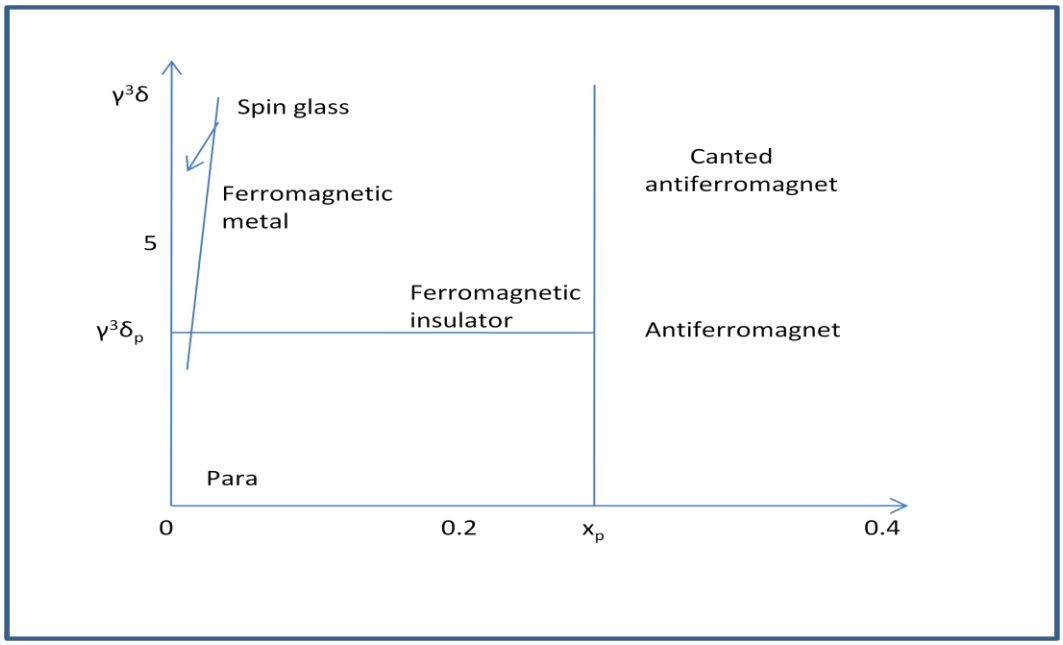

Figure 2.3. The magnetic phase diagram for oxide-based diluted magnetic semiconductors.[29]

spin-glass at higher densities since the interaction provides as many negative as positive exchange bonds.

It must be noted that despite the existence of the above theoretical models,[26,28,29] there is no exact explanation for the occurrence of ferromagnetism in DMS materials; although, itinerant carrier mediation between the localized 3d electron spins of the transition metal seems to be commonly regarded as the most likely source of ferromagnetism (Fig. 2.4).

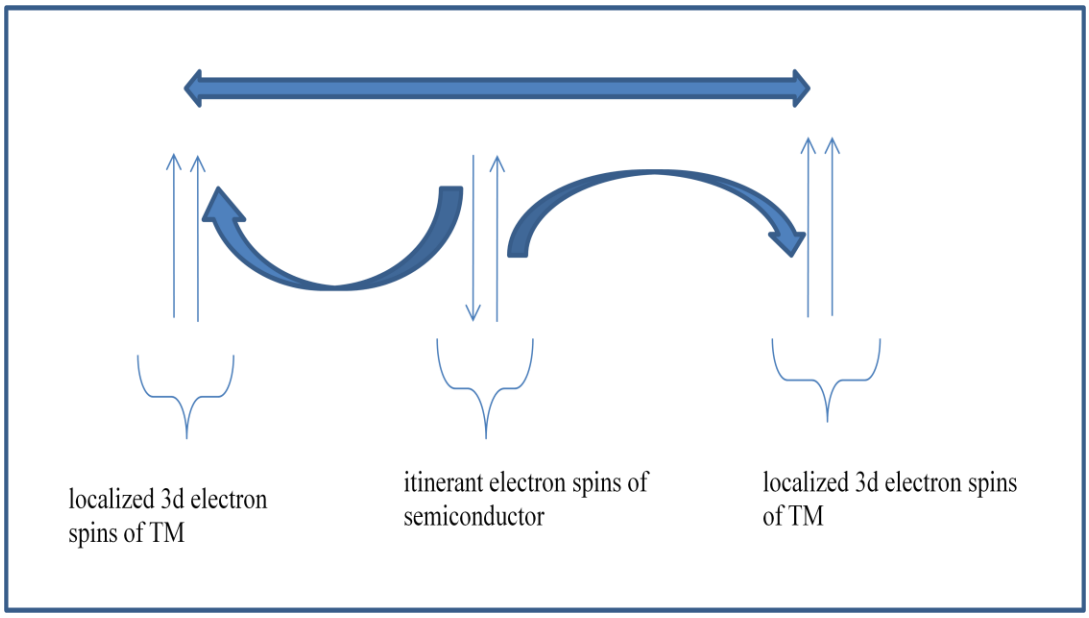

Figure 2.4. Schematic diagram of carrier-mediated ferromagnetism in DMS.

In this chapter, summarized statements about semiconductors, charge transport in semiconductors, magnetism and magnetic materials, and various theoretical models relevant in the explanation of ferromagnetism in DMS have been presented.

CHAPTER 3

GROWTH AND CHARACTERIZATION

3.1 Pulsed laser deposition

Pulsed laser deposition (PLD) is a deposition technique whereby a pulsed laser beam focused down by a lens hits a target of the desired material and creates a plume of the material perpenducular to the target surface. Typical lasers employed include ArF, KrF excimer lasers, and Nd:YAG laser. The PLD set-up in our laboratory used in this work has a KrF excimer laser source (Lambda Physik COMPex) and a high vacuum system that can attain pressures up to 10^{-7} mbar with the aid of roughing and turbo pumps. PLD has been very effective in the deposition of thin films of many materials especially complex oxides. Our high vacuum deposition system (Fig. 3.1) comprises a deposition chamber, target carousel with six target holders, a variable temperature

Figure 3.1. PLD system showing the laser and growth chamber in PAMS laboratory at Missouri State University.

substrate holder, and many standard ports such as pumping ports, gas inlet, pressure gauge, and view ports. Different parts are indicated in Fig. 3.2: the laser port, L; the target port flange-to-beam focal plane distance, Z; the target to substrate distance, S, and the substrate-to-flange distance, T. The target-to-substrate distance is usually about 5–15 cm. PLD involves a complex physical process of the interaction of high-power pulsed radiation on a solid target with the laser material, the formation of plasma plume, and the transfer of the ablated material through the plasma plume onto the substrate surface. Hence, pulsed laser deposition of thin films could be broken down into four different steps:

(a) Interaction of the laser radiation with the target

(b) Ablation materials dynamics

(c) Deposition of the ablated materials onto the substrate

(d) Thin film growth and nucleation on the substrate surface

The first step involves a focusing of the laser beam onto the surface of the target, and subsequent stoichiometric dissociation and ablation of the target material from the target surface. Various complex physical phenomena such as collisions, heating, electronic excitation etc, accompany the ablation process.

The second step involves a movement of the dissociated materials from the target towards the substrate as governed by the laws of gas-dynamics. The uniformity of the deposited film on the substrate is affected by the spot size of the laser and the plasma temperature. Also the angular spread of the ablated materials depends on the target-to-substrate distance.

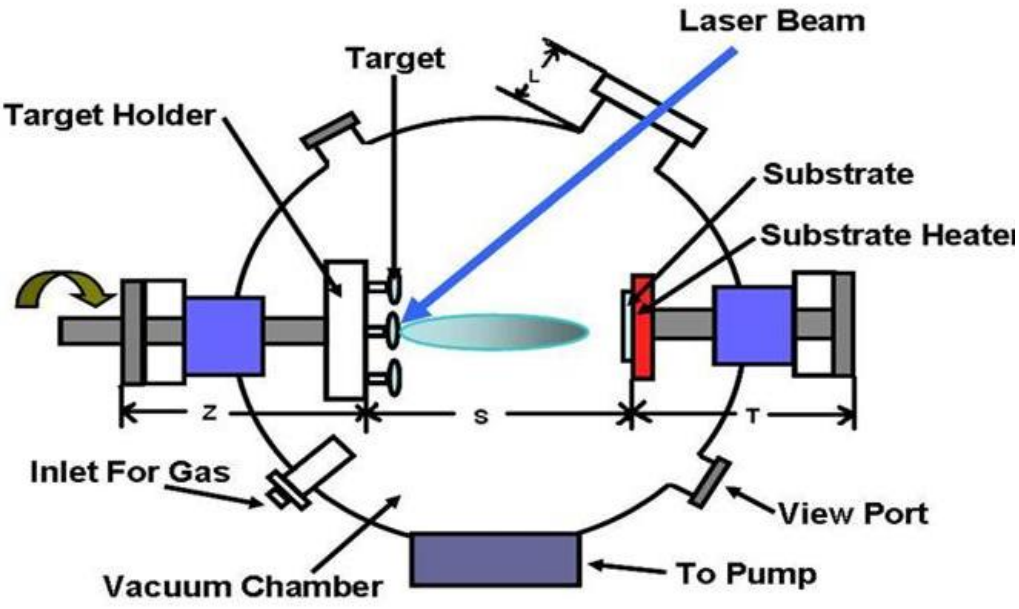

Figure 3.2. Schematic diagram of a pulsed laser deposition system.

In the third step, the emitted high-energy species impinge on the substrate surface. This step is critical in determining the quality of the film. Here, some of the surface atoms are sputtered by the energetic species, and this leads to the formation of a collision region between the incident flow and sputtered atoms; films grow only on the formation of a thermalized region.

The growth and nucleation step is a critical step which depends on such factors as the energy of the laser, density, ionization degree, and temperature as well as physical and chemical properties of the substrate. The growth of crystalline films is dependent on the surface mobility of the adatom, which diffuses through several atomic distances before settling at a stable position within the film. The adatom's surface diffusion mobility is dependent on the substrate temperature; it turns out that high temperature favors fast and defect-free crystal growth while amorphous or disordered structures are

favored by low temperature. The nucleation process depends on the interfacial energies between the substrate, condensing material, and vapor. The advantages of PLD over other deposition systems are: versatility, ability to maintain stoichiometry, low cost, ease of operation and cleanliness. Due to limited laser spot size, the ablation plume cross-section is usually small; this limits the sample size and causes thickness non-uniformity. The high forward direction of the plume of the ablated material makes thickness monitoring difficult.

3.2 Raman spectroscopy

Raman spectroscopy is a structural characterization tool at molecular level, which gives information about the structural properties of a material. It is based on the theory that photons of light on interaction with matter may be absorbed or scattered or may not interact with the material and may pass through it. In Raman scattering, the light interacts with the molecule and polarizes the electron cloud round the nuclei, and this electron cloud forms a short-lived state referred to as a virtual state. Elastic/Rayleigh scattering arises when the photons are scattered with very small frequency changes causing a mere distortion of the electron cloud. In Raman/inelastic scattering, the energy of the scattered photon is different from the incident photon by one vibrational unit of energy. Here, the scattering process induces nuclear motion, and energy is transferred either from the incident photon to the molecule or from the molecule to the scattered photon.

From Fig. 3.3, the Raman scattering process from the ground vibrational state, m results in absorption of energy by the molecule and its promotion to a higher excited state, n. This is referred to as Stokes scattering. However, due to thermal energy, some

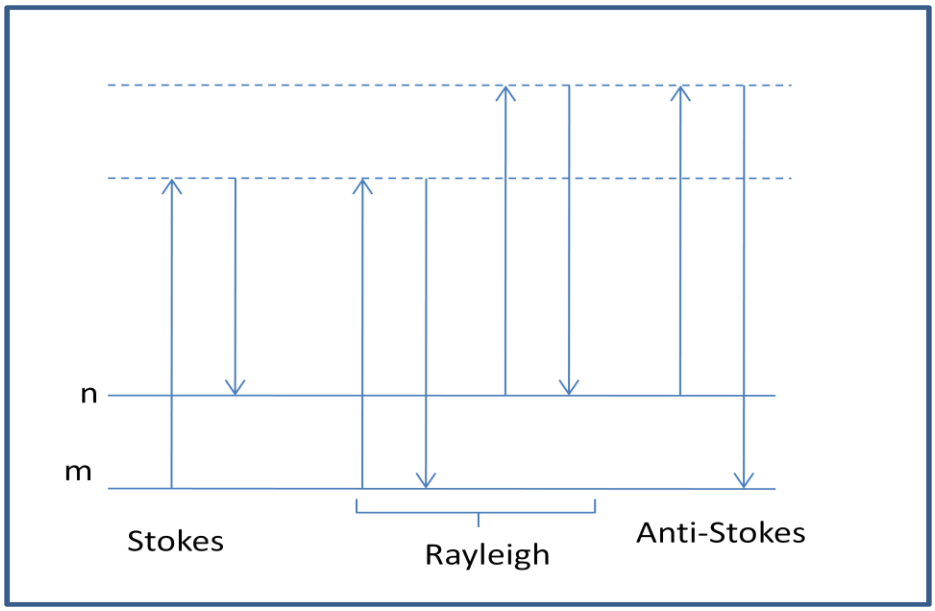

Figure 3.3. Schematic diagram of the Rayleigh and Raman scattering processes.

molecules may be present in an excited state such as n, and scattering from these states to the ground state, m is referred to as anti-Stokes scattering. A TRIAX 320 model system was used for the Raman measurement. This setup makes use of green laser as a light source. The back scattered light will be sent to a Charge Coupled Device (CCD); the green filter blocks the light with same wavelength as that of incident light. The remaining scattered light is analyzed by plotting a graph with the intensity (a.u.) along the y-axis and change in wave number (cm^{-1}) along the x-axis.

3.3 UV-visible spectroscopy

UV-visible spectroscopy gives information about the optical transmittance/absorbance as well as the band gap of a material. It enables a comparison of the measured intensity, I of a monochromatic light passing through a sample (liquid or soild) to the original intensity, I_0 of the incident light beam. A spectrophotometer is composed of a light source, a sample holder (with a cover to prevent outside light from

altering data) and a light detector. Here, light is passed through the desired sample for measurement, and the data (transmittance or absorbance) are collected with the aid of the Ocean Optics software. If no light is absorbed by the sample, $I = I_0$. $I < I_0$ implies absorption. Transmittance, T is the ratio of transmitted light to the incident light.

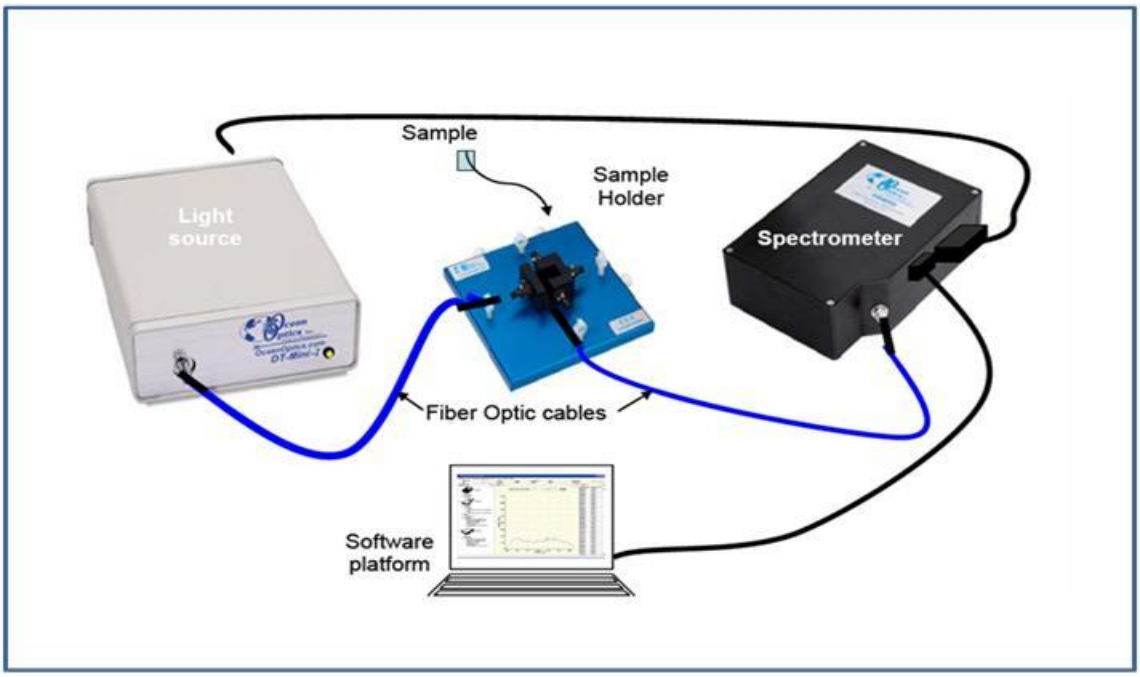

Figure 3.4. The UV-visible spectrophotometer set-up in PAMS laboratory at Missouri State University.

3.4. X-ray diffraction

X-ray diffraction is an important and non-destructive technique employed in semiconductor characterization. It enables the extraction of such information as structural quality, orientation, composition and lattice parameters. Fundamental theories and principles of operation were based on the works of W. H Bragg and W. L Bragg which were consolidated by more detailed and thorough descriptions in the 1940s by Laue and Ewald. A Bruker AXS Discover 8 (D8) diffractometer was used in this work. As with almost all high resolution-XRD (HRXRD) systems, it is made up of five basic parts: the

X-ray source, primary optics, sample holder, secondary optics and detector. It is also equipped with a computer-controlled goniometer that makes a perfect optimization of the scattering angles – incidence, reflection and rotation angles. Both double-crystal (with analyzer crystal) and triple axis (without analyzer crystal) are available. The source generates X-rays via electron transitions involving deep levels and the mostly used transition is the $K\alpha_1$ of Cu with a wavelength of $\lambda_{Cu}^{K\alpha_1}$ = 1.5405980 Å; although, other wavelengths which are filtered out with the aid of the secondary optics could also be generated in copper. The primary source could be a Ge (220) monochromator which collimates the Cu-tube X-ray incident beam. Figure 3.5 below is an illustration of the directions of the incidence and diffracted X-rays relative to the sample surface during a typical X-ray diffraction measurement. The symbol, ω, is the angle between the incident beam and the sample surface; and 2θ is the angle between the incident beam and the detector. Azimuthal rotations of the detector and sample about the axis in diffraction plane are represented by the angles φ and ψ respectively. Typical measurement scans involve a relative movement of the source and detector, and this differentiates one scan from another. In the ω-scan (rocking curve), the sample is rotated around the ω-axis with the x-ray and detector positions (2θ) fixed. For the 2θ/ω scan, the angles are changed so that θ = ω during the measurement. The lattice parameters of both sample and substrate could be obtained from the peak positions in the 2θ/ω scan. Information about the crystalline quality of semiconductor layers are extracted from the full-width at half maximum (FWHM) of ω-scans. Also, indications of the strain states of epitaxial layers are obtained by studying both the symmetric and asymmetric reflections since they give information about the in-plane and out-of-plane lattice constants. Reciprocal space maps

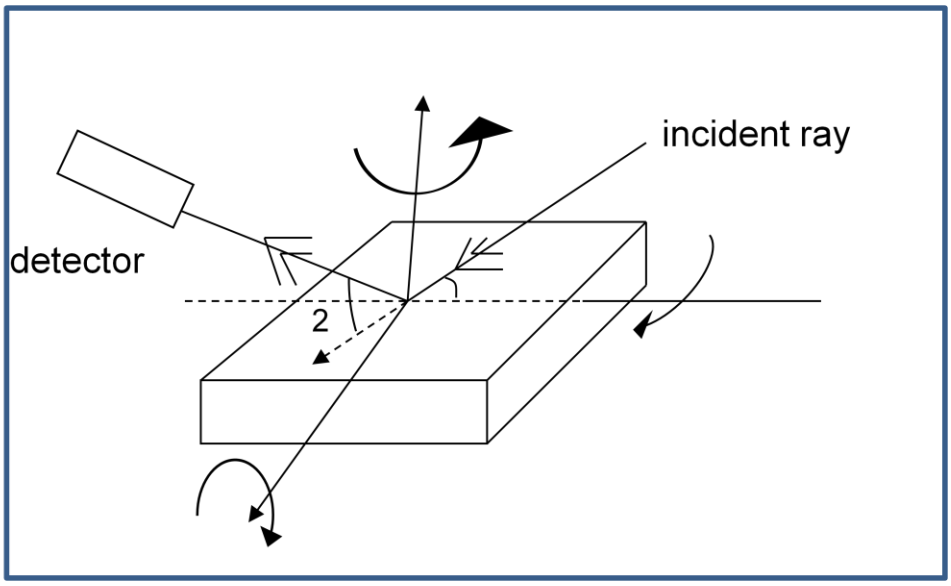

Figure 3.5. Schematic diagram of an X-ray diffractometer with associated movements and angles.

are preferred for more accurate analysis of strained/relaxed heterostructures.

3.5 Atomic force microscopy

Atomic force microscopy (AFM) is a highly sensitive method which mechanically gives information about the surface morphology with atomic scale resolution. AFM measurements in this work were carried out with the aid of the Veeco Dimension 3100 at CASE, Missouri State University. The basic idea in AFM is to let a sharp tip scan the surface of the sample. A small force applied to the tip moves the tip across the surface resulting in a variation in force between the tip and the surface atoms. The tip is mounted on a cantilever and the force causes it to deflect. The deflection is usually measured by a laser beam which is reflected in different angles depending on the degree of deflection. The actual force can then be calculated using Hooke's law, $F = -kz$; where F is the force, K is the cantilever spring constant and z is the displacement of the cantilever. A piezoelectric system is used to move the tip across the surface with high precision. The

AFM has three different modes of operation: contact mode, non-contact mode and tapping mode. The tapping AFM mode described below was used in this investigation. In this mode as the name implies, the tip taps the surface. The tip is set in motion, oscillates at or close to the resonance frequency and moves with an amplitude typically > 20 nm. Starting away from the surface, the tip is slowly brought in contact with the surface, tapping the surface atoms. An energy loss to the surface atoms and a decrease in amplitude occur due to the tapping. A feedback loop keeps the amplitude and force, constant by adjusting the separation during movement.

3.6. Hall effect

The Hall effect measurement is a common technique employed in the characterization of semiconductors, and was majorly used in this work. The Hall measurement gives information about free carrier concentration, type of carriers and mobility of carriers. It works on the principle that a Lorentz force is experienced by charge carriers in a semiconductor sample when a magnetic field is applied transversely to the direction of current flow. As a result, the carriers are pulled to one side of the sample leading to a buildup of an electric field which is measured as the Hall voltage, E_Y.

$$E_Y = R_H . J_X . B_Z \qquad (3.1)$$

In carrying out Hall effect measurements on our samples, the Van der Pauw approach was used due to its apparent advantages and accuracy in results. The Van der Pauw approach removes the problem of making symmetrical pieces and sample dimension uncertainties. It only requires that the samples be flat, isotropic and homogenous. Although the geometry could be arbitrary, 3 mm x 3 mm samples were used in the measurements with four indium contacts made at the edges as shown in figure 3.5 (b).

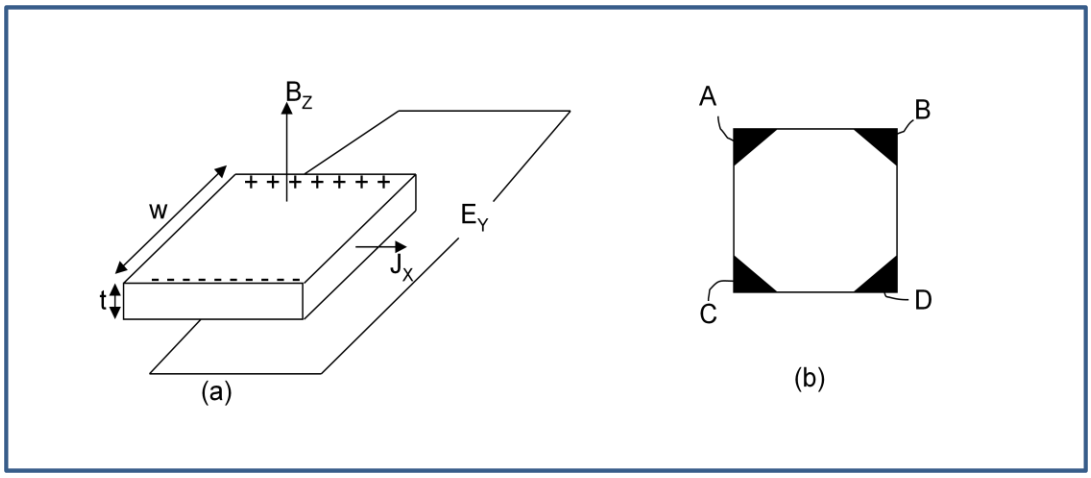

Figure. 3.6. Schematic diagram of (a) Hall effect (b) Van der Pauw configuration.

By passing current through neighboring contacts (A ↔B, B ↔ C, C↔ D, D↔ A) and measuring the voltages across the remaining, the resistivity ρ, as well as the resistance, $R_{AB,\ CD}$, given by,

$$R_{AB,CD} = \frac{V_D^0 - V_C^0}{i_{AB}} \tag{3.2}$$

are obtained. The zero superscript indicates that no magnetic field is applied. From the two characteristic resistances, $R_{BC,DA}$ and $R_{AB,CD}$ and analyzing the field distribution, Van der Pauw showed that the resistivity ρ, could be obtained thus:

$$\exp\left(\frac{-\pi d}{\rho} R_{BC,DA}\right) + \exp\left(\frac{-\pi d}{\rho} R_{AB,CD}\right) = 1 \tag{3.3}$$

With the initial application of a magnetic field, B followed by passing a current through neighbouring contacts (A ↔C, B↔ D) and measuring of Hall voltage across the remaining contacts, Van der Pauw analytically obtained an expression for the Hall coefficients, $R_{H.}$

$$R^{H}_{AC,BD} = \frac{d}{|B|} \cdot \frac{V_2^B - V_4^B}{i^B_{AC}} = \frac{d}{|B|} . R^B_{AC,BD} \tag{3.4}$$

The charge carrier concentration, n and the carrier mobility, μ_H were obtained as shown in equations (3.5) and (3.6) below respectively.

$$\text{n} = \frac{1}{qR_H} = \frac{|B|}{qdR_{AC,BD}} \tag{3.5}$$

$$\mu_H = \frac{R_H}{\rho} = \frac{dR_{AC,BD}}{\rho|B|} \tag{3.6}$$

All the samples were measured in the 5 – 300 K temperature interval using the low temperature system with an applied magnetic field of up to 1.3 T.

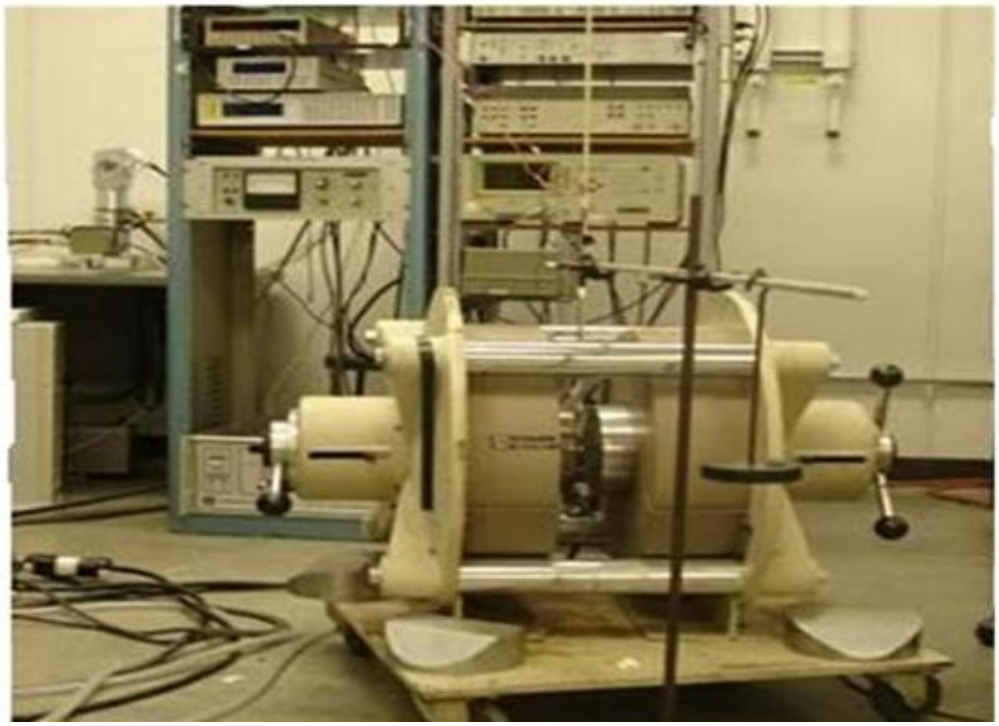

Figure 3.7. The Hall effect set-up in PAMS laboratory at Missouri State University.

3.7. Temperature dependent resistivity

Just like in Hall effect, temperature dependent resistivity measurements were carried out using the four-probe electrical measurement technique. The temperature-dependent resistivity measurements were carried out in the 50 – 300 K temperature range. The current was supplied via the Keithley 230 current source and the voltage was read off using the Keithley 182 voltmeter. The resistivity of the samples can be calculated using the relation

$$\rho = \frac{RA}{L} \tag{3.7}$$

where R is the measured resistance value, and A is the cross-sectional area of sample and L is the length.

3.8 SQUID magnetometry

It turns out that magnetic measurements are the key tool for characterizing our samples. DC magnetic measurements determine the equilibrium value of the magnetization of the sample, while AC magnetic measurements give information on magnetization dynamics that are not obtainable via DC measurement. This characterization was carried out with the aid of superconducting quantum interference device (SQUID) magnetometer. Here, the dependence of the magnetization (M) of the sample on temperature at applied magnetic field (FC) was measured, with the field usually set at 1000 Oe. Such information like Curie and Neel temperatures can be obtained from this measurement. This was followed by measurements of the magnetization at changing magnetic field usually at temperatures of 5 K, 100 K, and 300 K. From these measurements, information about hysteresis effects and saturation magnetization are obtainable. The applied magnetic field ranged from 0 to 5 T.

3.9 Samples

Cr-doped Indium oxide was chosen to study DMS properties for the following reasons: indium oxide belongs to the family of transparent oxide semiconductors; although not as well investigated as other transparent semiconductors. Indium oxide crystallizes in the cubic bixbyte structure, with a band gap of 3.75 eV, and lattice constant of 10.118 Å.[19] It is possible for indium to occupy two positions in the lattice – the octahedral and tetrahedral positions. The oxygen positions also could have vacancies, which usually gives rise to n-type conductivity in indium oxide. Indium oxide (In_2O_3) is a transparent, n-type material with inherent oxygen deficiencies whose electrical and optical properties can be effectively tuned by tuning the oxygen vacancies through chemical doping as well as growth parameters such as partial oxygen pressure in the growth chamber and substrate temperatures.

Chromium belongs to the family of transition metals. It is antiferromagnetic in the bulk state, and superparamegnetic in small cluster form. CrO_2 is the only ferromagnetic secondary phase of chromium. Compared with most transition metals, Cr has large magnetic moment in the ionic state, and unlike Co, observation of ferromagnetism due to Cr clustering is ruled out since small amounts of Cr clusters result in superparamagnetism while bulk Cr is antiferromagnetic.

A chromium-doped indium oxide (In_2O_3:Cr) target with 2.5 wt % chromium was prepared by standard solid-state reaction method using high purity In_2O_3 (99.999 %) and Cr_2O_3 (99.8 %). Required amounts of In_2O_3 and Cr_2O_3 were taken by molecular weight and mixed thoroughly. The well-ground mixture was heated in air at 800 ˚C for 12 h. The powder mixture was cold-pressed using a hydraulic press at 15 tons load, and sintered in

air at 800 ˚C for 12 h. The sapphire substrates were dropped in propanol and ethanol respectively and put in an ultrasonic cleaner for approximately 5 mins to ensure proper cleaning. Cr-doped In_2O_3 thin films were grown on the c-plane sapphire substrates using pulsed laser deposition (PLD) technique (KrF excimer laser, λ=248 nm) for ~ 20 min at a substrate temperature of 400 ˚C. The laser was operated at a pulse rate of 10 Hz and energy of 300 mJ/cm^2. The deposition chamber was initially evacuated to a base pressure of ~ 3.0×10^{-6} torr, followed with the introduction of oxygen gas in order to obtain the required growth pressures of 7.5×10^{-6} (Sample A), 7.5×10^{-5} (Sample B), 7.5×10^{-4} (Sample C), and 7.5×10^{-3} (Sample D) torr. Details of growth parameters of samples are given in Table 3.1.

Table 3.1. Summary of In_2O_3:Cr films growth parameters

Sample	Substrate	Growth Temperature (C)	Atmosphere	Chamber Pressure (Torr)
A	Sapphire	400	Oxygen	7.5×10^{-6}
B	Sapphire	400	Oxygen	7.5×10^{-5}
C	Sapphire	400	Oxygen	7.5×10^{-4}
D	Sapphire	400	Oxygen	7.5×10^{-3}

Results of samples A, B, C, and D contained in this report are representatives of four batches of samples grown under similar conditions and observed to exhibit similar property trends. All samples were characterized with the Bruker AXS x-ray diffractometer using CuK_α radiation having a wavelength of 1.5406 Å. The surface

morphology of the films was investigated using atomic force microscopy (AFM). The thickness of the films were measured using atomic force microscopy and found to be 58 nm, 53 nm, 46 nm, and 41 nm for samples A, B, C, and D respectively. Micro-Raman scattering experiments were also performed in perfect back-scattering geometry using a fiber-optically coupled confocal micro-Raman system. The optical transmittance measurements were carried out using ultra-violet visible spectrophotometer (Ocean Optics HR400). The resistivity and Hall effect measurements were carried out using the standard four-probe technique. All film resistivity was obtained from the average of measurements for each film. The magnetic field dependence of Hall effect was measured with the field applied perpendicular to the film surface in the Van der Pauw configuration. The Hall voltage was measured using a Keithley 182 voltmeter and current was supplied using the Keithley 230 current source. Magnetization characterizations on the films were carried out with the aid of the SQUID magnetometer. This chapter highlights the various film growth and characterization equipment and techniques used in this work. It also contains a summary of the sample growth parameters.

CHAPTER 4

RESULTS AND DISCUSSIONS

4.1. Structural properties

In_2O_3 crystallizes in the cubic bixbyte structure with a lattice constant of 10.118 Å and a direct band gap of 3.75 eV.[19] The diffraction peaks (samples A-D) in Fig. 4.1 are for In_2O_3:Cr samples grown at 7.5×10^{-6}, 7.5×10^{-5}, 7.5×10^{-4}, and 7.5×10^{-3} torr of partial oxygen pressure on sapphire substrates. The films are highly crystalline and in good agreement with the JCPDS file card no. 06-0416 for In_2O_3, all the films show peaks corresponding to In_2O_3 phase only, which suggests that Cr forms a solid solution with In_2O_3 in all our samples. It could be seen from Fig. 4.1 that not all the peaks are present, possibly due to the preferential orientation of the films in the (222) plane. The peaks labeled 'S' correspond to the substrate. From Fig. 4.2, one notices an obvious shift of the diffraction peaks to lower angles with increasing partial oxygen pressure, which indicates an expansion in the lattice constant. Using the relations

$$\lambda = 2d_{hkl} \sin \vartheta \tag{4.1}$$

and

$$d_{hkl} = \frac{a}{\sqrt{h^2 + k^2 + l^2}} \tag{4.2}$$

for cubic structures, where λ is diffraction wavelength, d_{hkl} is the interplanar distance, and ϑ is the diffraction angle, an increase in lattice constant from 10.103 Å to 10.337 Å as the oxygen growth pressure increases from 7.5×10^{-6} to 7.5×10^{-3} Torr was observed as shown in Fig. 4.3. For sample A, it could be explained that the lattice distortion and

consequent lower lattice constant value (10.103 Å) when compared with In_2O_3 (10.118 Å), is due to the incorporation of smaller Cr ions into the In sites of the In_2O_3 lattice.[19]

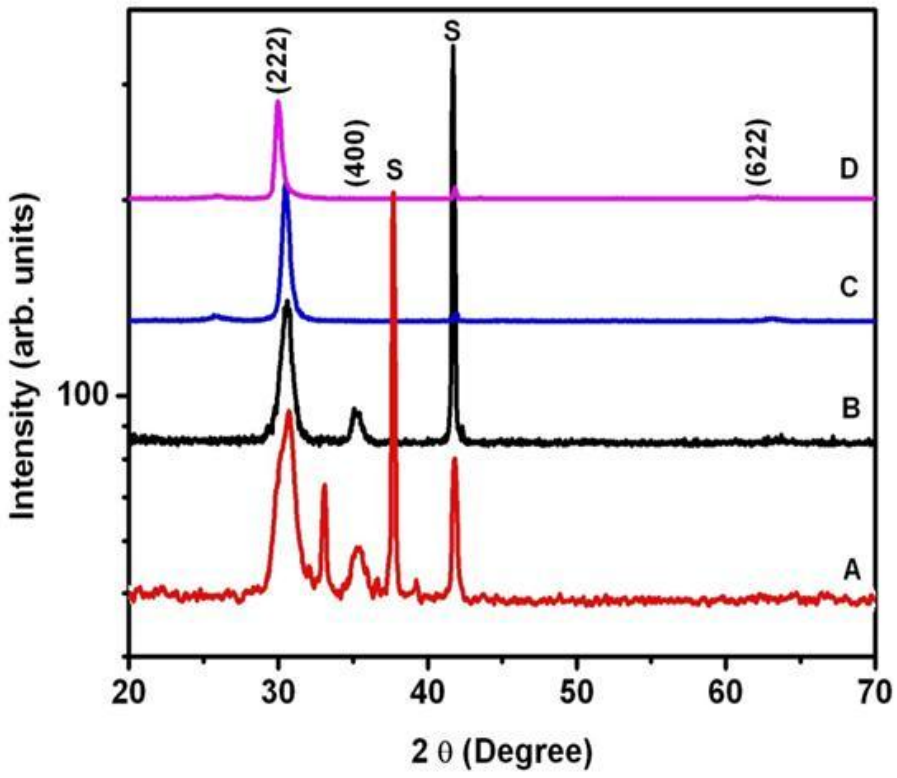

Figure 4.1. X-ray diffraction pattern for films grown at partial pressures of (A) 7.5×10^{-6}, (B) 7.5×10^{-5},(C) 7.5×10^{-4}, and (D) 7.5×10^{-3} Torr of oxygen.

A broadening of the (222) diffraction peaks due to the effects of strain and/or size, is also noticeable from Fig. 4.2. Sherrer method was employed to estimate the particle sizes of the thin films using the relation[33]

$$t = \frac{C\lambda}{\beta \cos \vartheta} \qquad (4.3)$$

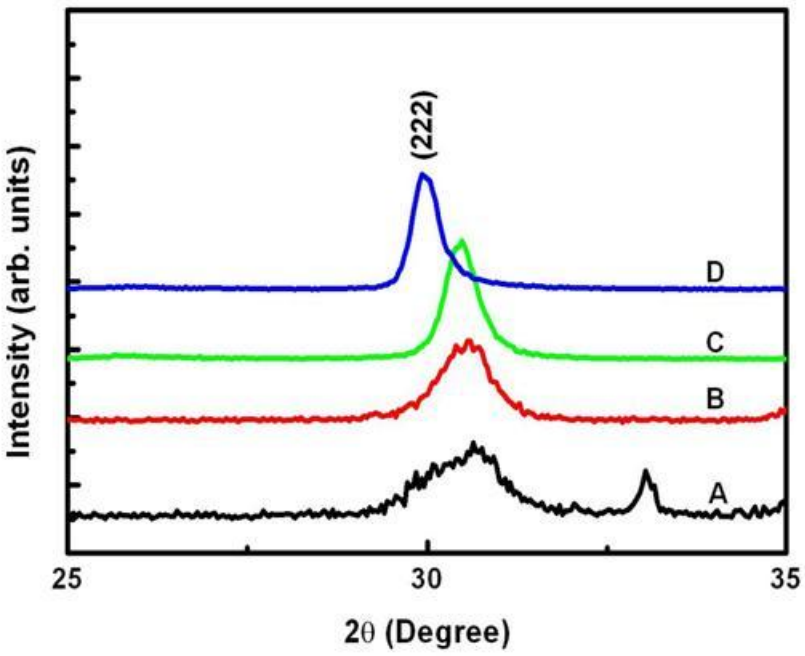

Figure 4.2. X-ray diffraction pattern for films grown at partial pressures of (A) 7.5×10^{-6}, (B)7.5×10^{-5},(C) 7.5×10^{-4}, and (D)7.5×10^{-3} Torr of oxygen expanded around (222). plane.

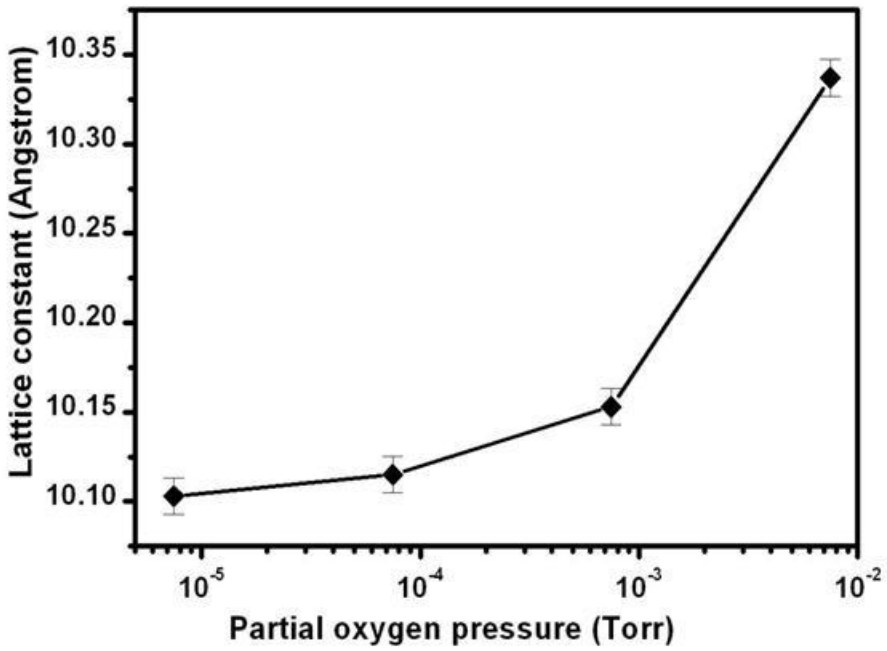

Figure. 4.3. Plot of lattice constant vs. partial oxygen pressure for In_2O_3:Cr films.

where β is the full width at half maximum (FWHM) of the XRD peak, λ is the x-ray wavelength, ϑ is the diffraction angle, and C is the correction factor which is taken as unity.

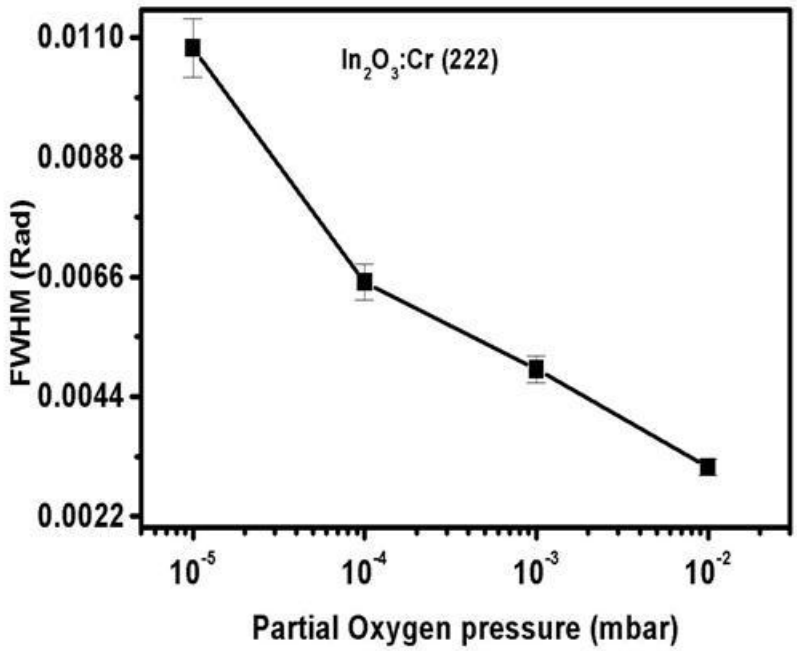

Figure 4.4. The effect of oxygen growth pressure on the crystal quality of In_2O_3:Cr films.

The estimated particle sizes were determined using the (222) diffraction peaks and are shown in Fig. 4.5. The particle size varies from 13.9 nm to 35.3 nm with increase in partial oxygen pressure. Tsunekawa et al.[31] have reported an observed anomalous lattice expansion with decreasing particle size in oxide nanoparticles. Z. D. Zhou et al.[32] have also correlated an observed lattice expansion and decrease in particle size in CeO_2 nanoparticles, with increased concentration of oxygen vacancies.

In this work, our observed lattice expansion and increase in particle size with increased partial oxygen pressure is proposed to be due to the reduction in oxygen

vacancies in these thin films. The shrinking of the full width at half maximum (FWHM) of the diffraction peaks with increase in partial oxygen pressure (Fig. 4.4) - an indication

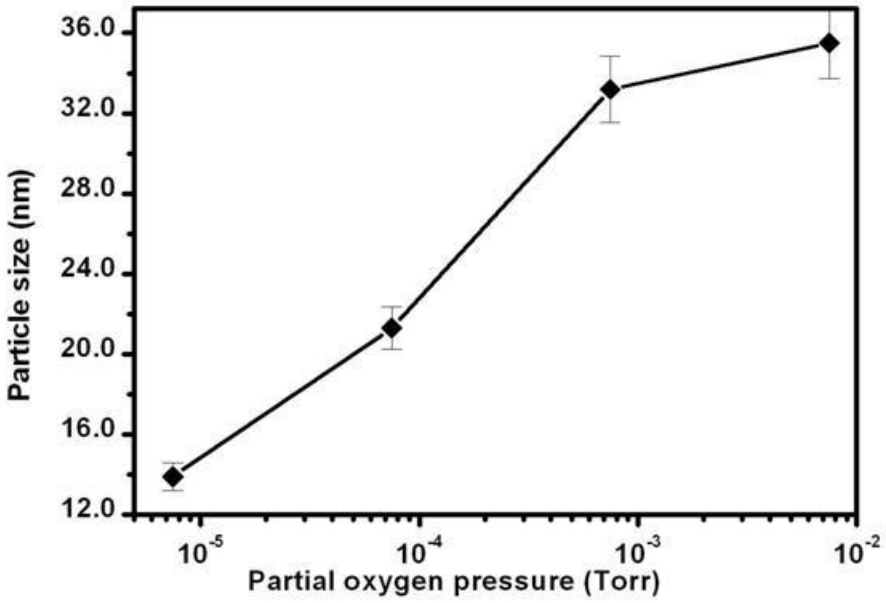

Figure. 4.5. Plot of particle size vs. partial oxygen pressure for In_2O_3:Cr films.

of improved crystallinity, independently supports the estimated particle sizes for the films. The FWHM of (222) decreases from 0.0108 rad to 0.0031 rad as the partial oxygen pressure increases from 7.5×10^{-6} to 7.5×10^{-3} Torr.

The Raman spectra for In_2O_3:Cr is shown in Fig. 4.6. The factor group analysis predicts the following modes for In_2O_3: $4A_g$ (Raman) + $4E_g$ (Raman) + $14T_g$ (Raman) + $5A_u$ (inactive) + $5E_u$ (inactive) + $16T_u$ (infra-red). Raman peaks corresponding to In_2O_3 were observed at 306.8, 366.8, and 496.3 cm^{-1}. Within an experimental accuracy of a few wave numbers, no discernible shifts in the sample peaks as a result of oxygen growth pressure were observed.

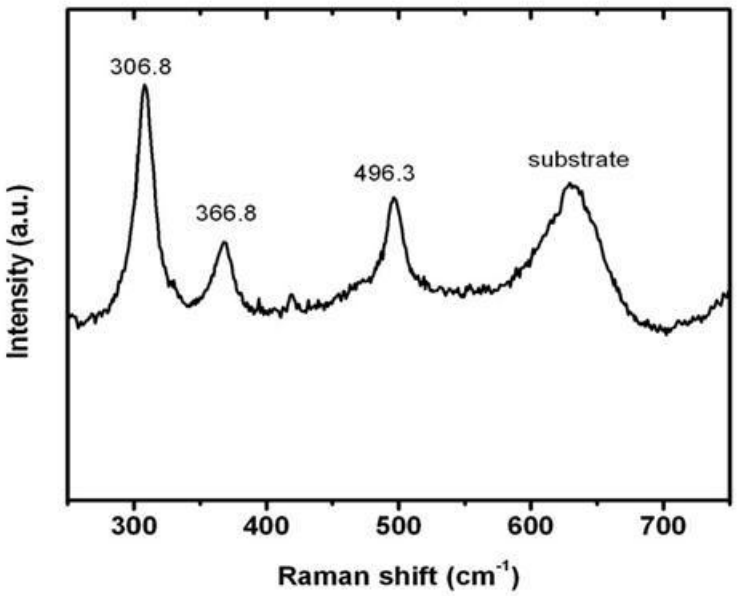

Figure 4.6. Raman spectra of Cr (2.5 %)-doped In_2O_3 films.

AFM measurements carried out on the samples show the smoothest surface for the sample grown at 7.5×10^{-4} Torr with a root mean square (rms) value of 1.7 nm (Fig. 4.9). The sample morphology is suggestive of island growth.

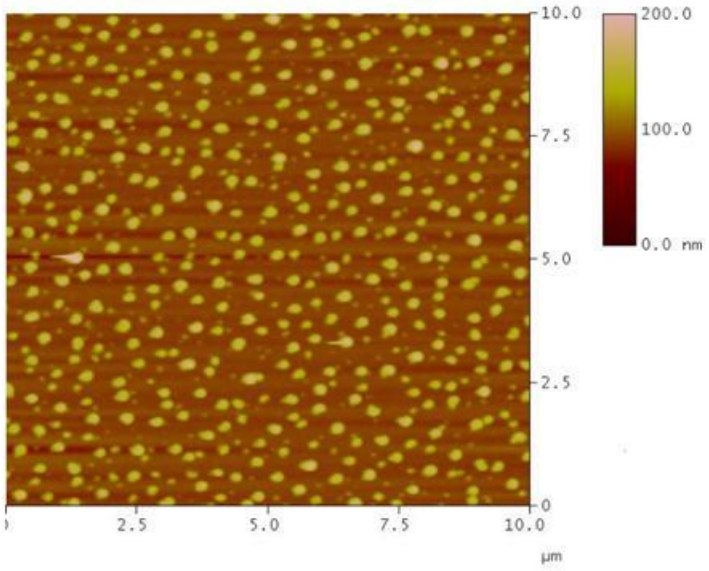

Figure. 4.7. AFM image for In_2O_3:Cr films grown at partial oxygen pressure of 7.5×10^{-6} Torr.

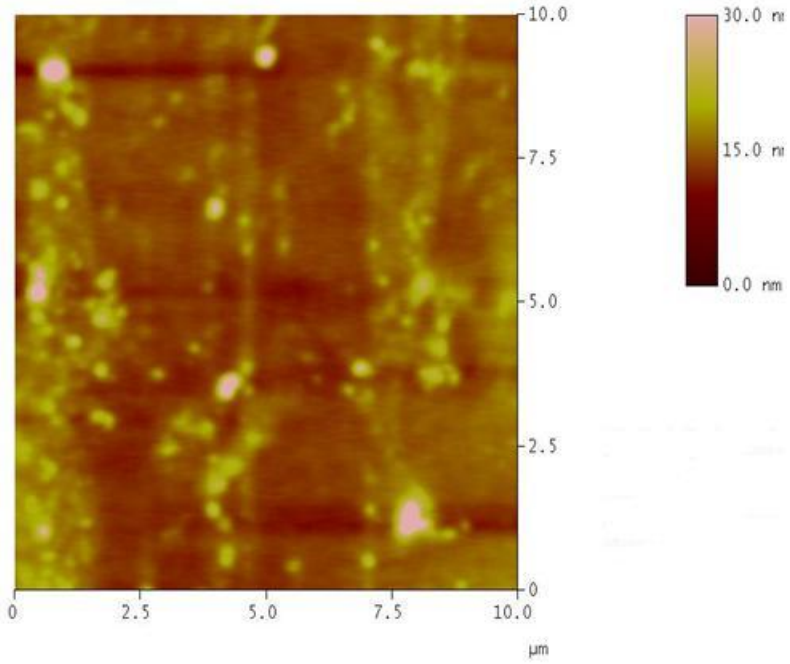

Figure. 4.8. AFM image for In_2O_3:Cr films grown at partial oxygen pressure of 7.5×10^{-5} Torr.

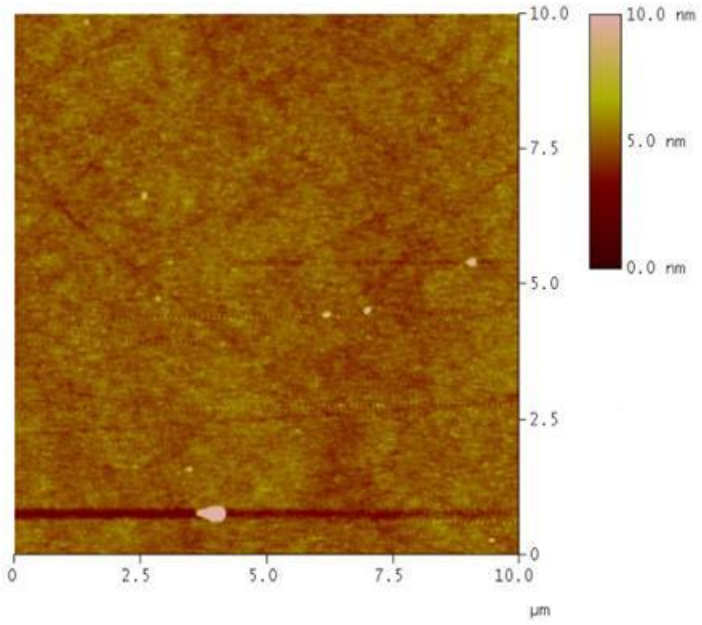

Figure. 4.9. AFM image for In_2O_3:Cr films grown at partial oxygen pressure of 7.5×10^{-4} Torr.

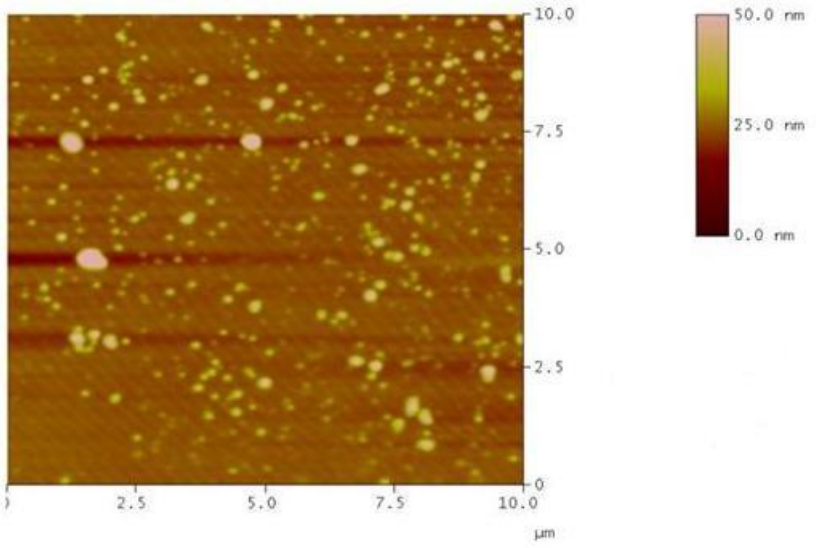

Figure. 4.10. AFM images for In_2O_3:Cr films grown at partial oxygen pressure of 7.5 × 10^{-3} Torr.

4.2. Optical properties

The optical transmission spectra of In_2O_3:Cr films are shown in Fig. 4.11. Optical transmittance is observed to be strongly dependent on the oxygen growth pressure. The films are highly transparent. The average optical transparency is observed to increase from ~ 52 % to ~ 85 % as the partial oxygen pressure increased from 7.5 × 10^{-6} to 7.5 × 10^{-3} Torr respectively. According to the Drude model,[33] the plasma frequency – responsible for the absorption peaks is given by

$$w_p = \frac{ne^2}{m\varepsilon_0} \qquad (4.4)$$

where e is the electron charge, n is the electron density, ε_0 is the permittivity in free space, and m^* is the electron effective mass. In order to explain the observed optical behavior of our films, we employed the ionized impurity scattering model due to heavy doping.

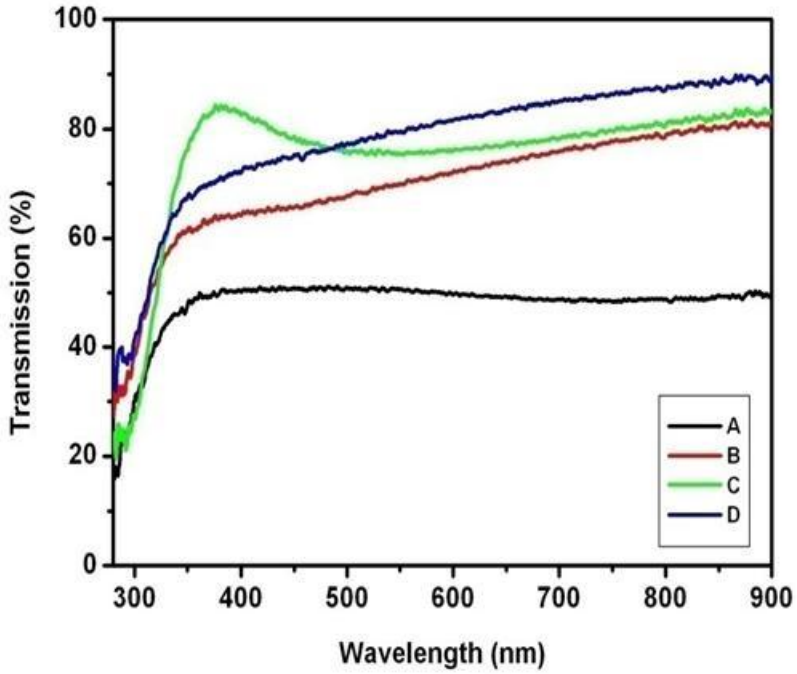

Figure 4.11. Optical transmission spectra of In_2O_3:Cr films.

Here, the frequency dependent relaxation time, which is usually introduced at $w > w_p / \sqrt{\varepsilon_\infty}$ is given by[33]

$$\tau^{IIS}(w) = \tau_0 \left(\frac{w_p}{\sqrt{\varepsilon_0}} \right)^{-3/2} w^{3/2} \qquad (4.5)$$

where $w_p / \sqrt{\varepsilon_\infty}$ is the screened plasma frequency. The decrease in the screened plasma frequency with increase in partial oxygen pressure, and consequent reduction in carrier concentration, results in increased relaxation time and reduced absorption. Hence, transparency is enhanced in the films as shown in Fig. 4.12. Figures 4.12 – 4.15 show the relationship between absorption coefficient and photon energy. Neglecting reflectivity near the absorption edge in the transmission spectrum, the optical transmittance (T) is given by[34]

$$T = T_0 \exp(-\alpha d) \tag{4.6}$$

where α and d are the optical absorption coefficient and the film thickness respectively. From Figs. 4.12 – 4.15, the energy band gap, E_g of the samples were estimated using the relation[34]

$$(\alpha h\nu)^2 = (h\nu - E_g) \tag{4.7}$$

where $h\nu$ is the photon energy. By an extrapolation of the linear region of $(\alpha h\nu)^2$ vs. $h\nu$ plot to the photon energy axis, the energy band gap, E_g can be obtained.

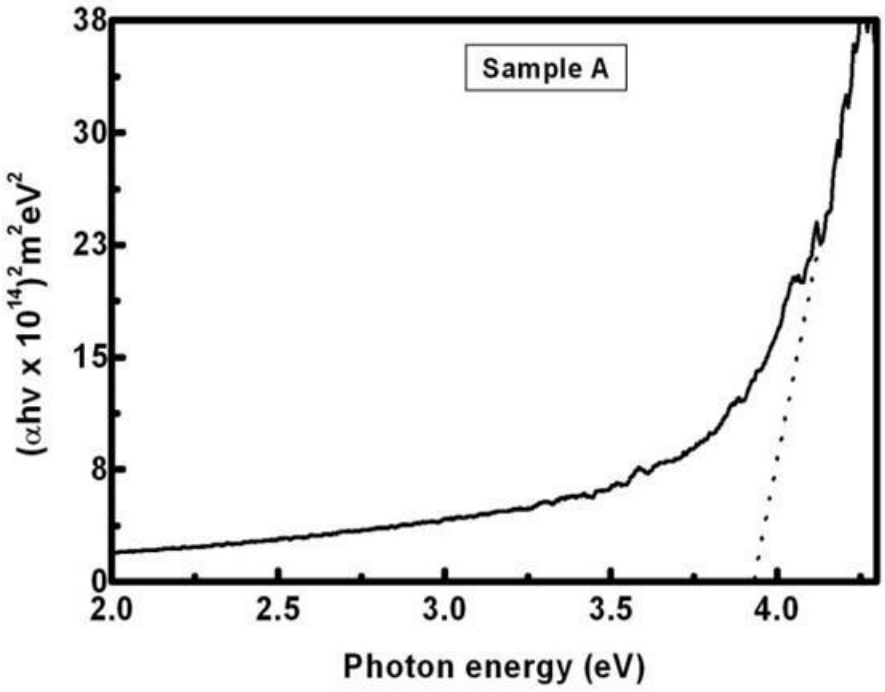

Figure 4.12. Plot of $(\alpha h\upsilon)^2$ vs. photon energy for In_2O_3: Cr film grown at 7.5×10^{-6} Torr.

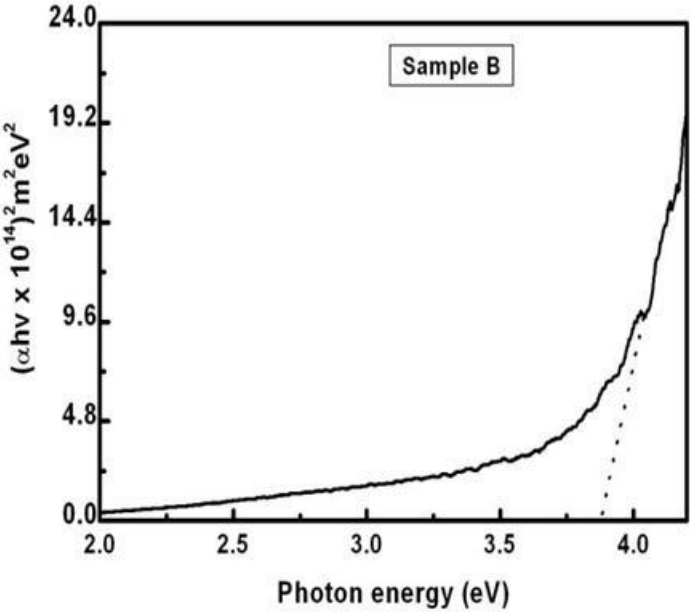

Figure 4.13. Plot of $(\alpha h\upsilon)^2$ vs. photon energy for In_2O_3: Cr film grown at 7.5×10^{-5} Torr.

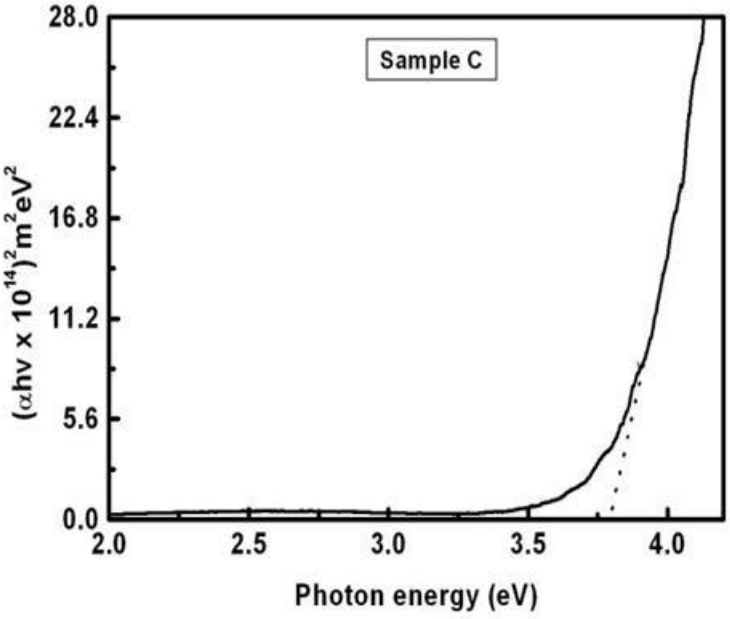

Figure. 4.14. Plot of $(\alpha h\upsilon)^2$ vs. photon energy for In_2O_3: Cr films deposited at partial oxygen pressure of 7.5×10^{-4} Torr.

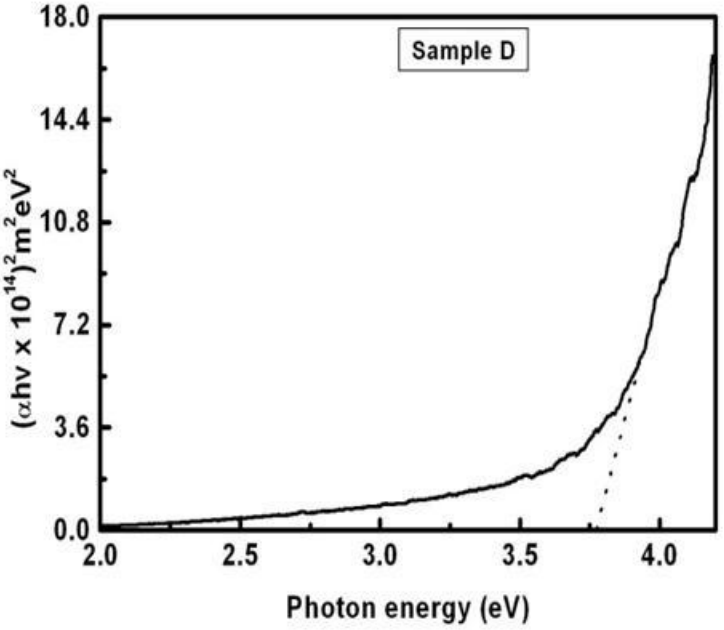

Figure. 4.15. Plot of $(\alpha h\upsilon)^2$ vs. photon energy for In_2O_3: Cr films deposited at partial oxygen pressure of 7.5×10^{-3} Torr.

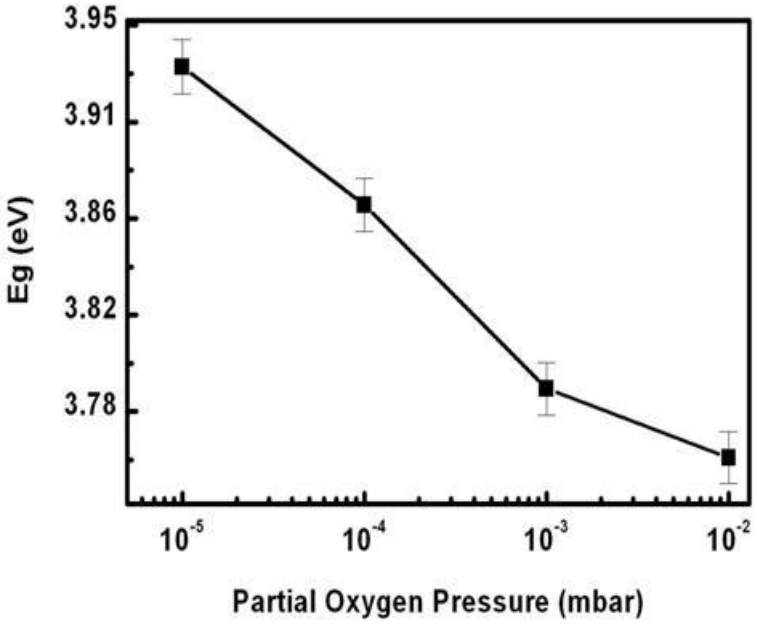

Figure 4.16. The variation of energy band gap with partial pressure of oxygen.

A redshift of the energy band gap with partial oxygen pressure is observable from Fig. 4.16. The observed decrease in the energy band gap from 3.93 eV to 3.76 eV is attributed to the improvement in the crystallinity and order in the films with increase in oxygen growth pressure as seen from the XRD analysis, and this, results in the reduction of the interatomic spacing as well as shifts of the absorption edges to longer wavelengths. Tan et al.[34] have proposed that an observed blue shift in the absorption edges of ZnO thin films with decrease in growth temperature is due to poor crystallinity, which gives rise to the absence of long-range periodicity, and increase in the extended localizations in the conduction and valence bands.

4.3. Magnetotransport properties

From Fig. 4.17, it could be noticed that the resistivity of the films increases as the oxygen growth pressure increases with resistivity as low as ~ 10^{-4} Ω cm. An improvement in mobility from 15 to 133 cm^2/Vs with increase in partial oxygen pressure from 7.5 × 10^{-6} to 7.5 × 10^{-3} Torr is observed. This observed increase in mobility is due to improvement in crystallinity and reduction in grain boundary scattering resulting from increase in grain size as corroborated by XRD analysis. The increase in resistivity of the films from 2.0 × 10^{-4} to 4.7 × 10^{-4} Ω cm with increase in partial oxygen pressure from 7.5 × 10^{-6} to 7.5 × 10^{-3} Torr is due to the reduction in the defect density, specifically oxygen vacancies. Magnetotransport properties of sample A (Hall resistance) were investigated with the magnetic field up to 1.5 T applied perpendicularly to the film plane in the 5 – 300 K temperature range. The Hall resistance gives an idea of the magnetic properties, the conduction type as well as the carrier concentration. It turns out that the Hall

resistance in ferromagnetic semiconductors can be expressed as the sum of the ordinary and anomalous Hall terms[35]

$$R_{Hall} = R_O B + R_S M \tag{4.8}$$

where R_O is the ordinary Hall coefficient, B is the magnetic field, M is the average

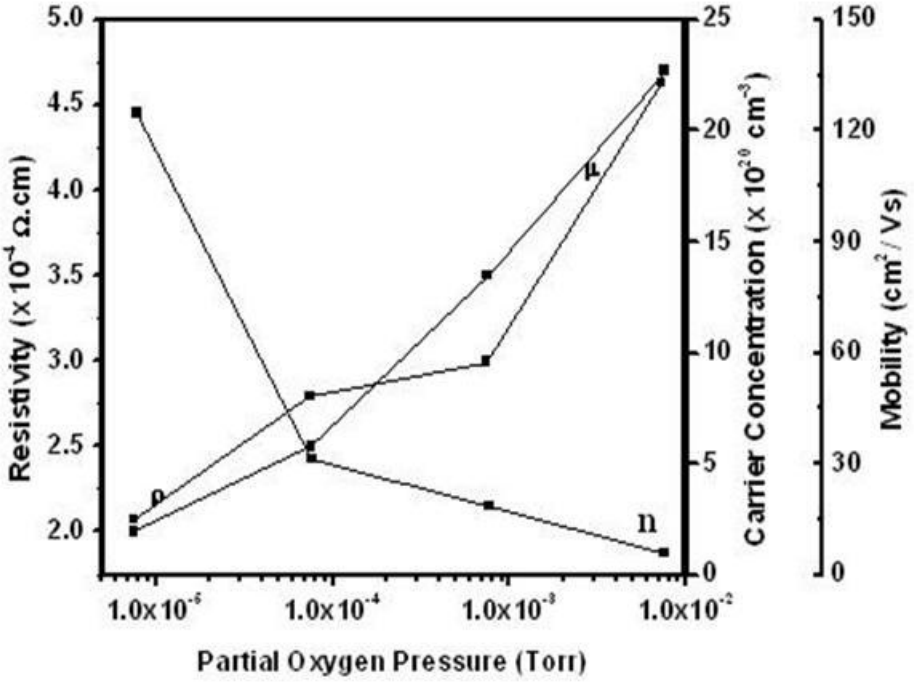

Figure 4.17. Effect of partial oxygen pressure on electrical (a) resistivity, (b) carrier concentration, and (c) mobility of In_2O_3:Cr films.

magnetization, and R_S is the anomalous Hall coefficient. From equation 4.8, unlike in the linear field dependence for ordinary Hall effect, the non-linear magnetic field dependence of the anomalous Hall effect is a signature of ferromagnetic ordering. Such an anomalous Hall resistance behavior – proportional to the perpendicular component of magnetization, was observed in our films up to 300 K as could be seen from the plots of temperature and magnetic field dependence of Hall resistance. The persistence of the non-linear magnetic field dependence of the Hall resistance even at 300 K (Figs. 4.18 - 4.21) suggests the

existence of ferromagnetism at room temperature in our film. The negative slope of R_{Hall} indicates that the charge carriers are n-type. No variation in carrier concentration with change in temperature was observed.

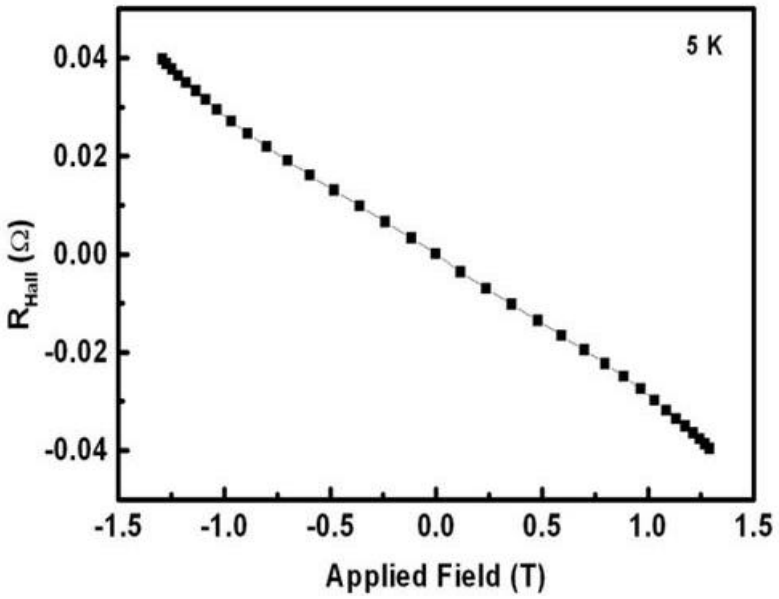

Figure.4.18. Hall resistance vs. magnetic field applied perpendicular to the plane of In_2O_3:Cr film (Sample A) at 5 K.

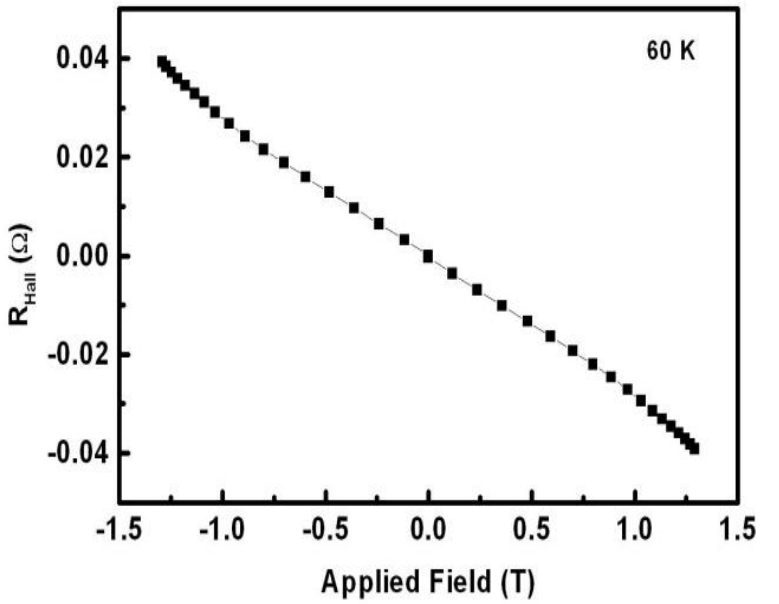

Figure 4.19. Hall resistance vs. magnetic field applied perpendicular to the plane of In_2O_3:Cr film (Sample A) at 60 K.

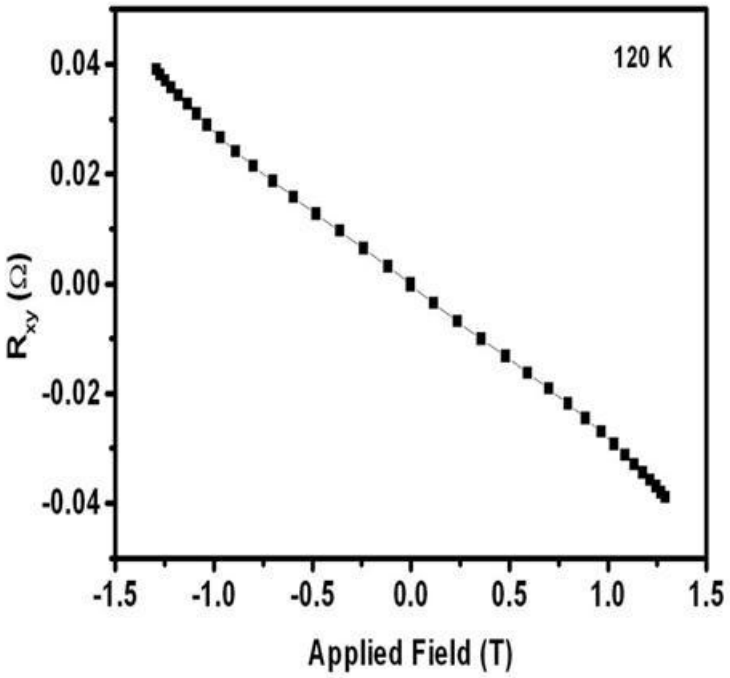

Figure 4.20. Hall resistance vs. magnetic field applied perpendicular to the plane of In_2O_3:Cr film (Sample A) at 120 K.

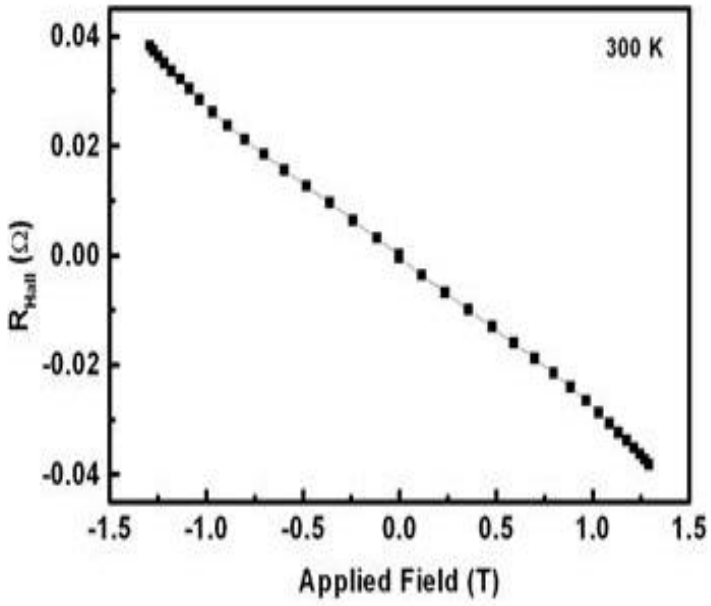

Figure 4.21. Hall resistance vs. magnetic field applied perpendicular to the plane of In_2O_3:Cr film (Sample A) at 300 K.

Temperature dependent resistivity measurements in the 45 < T < 300 K temperature interval for the films reveal interesting behaviors as could be seen from Figs. 4.22 – 4.25.

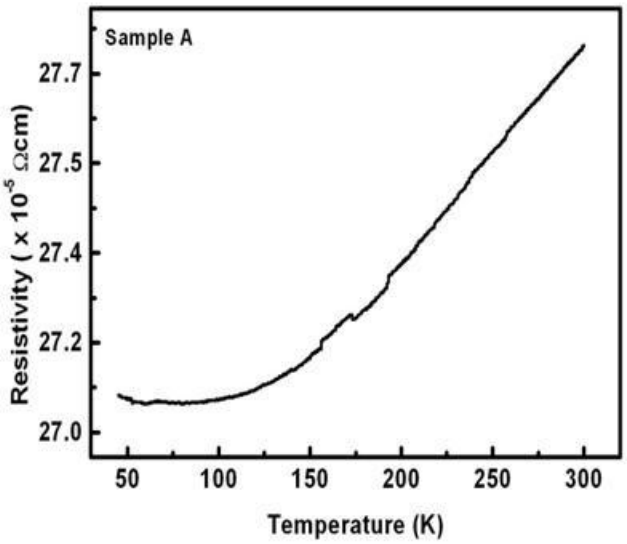

Figure 4.22. Resistivity vs. temperature plots for film grown at 7.5×10^{-6} Torr of oxygen pressure.

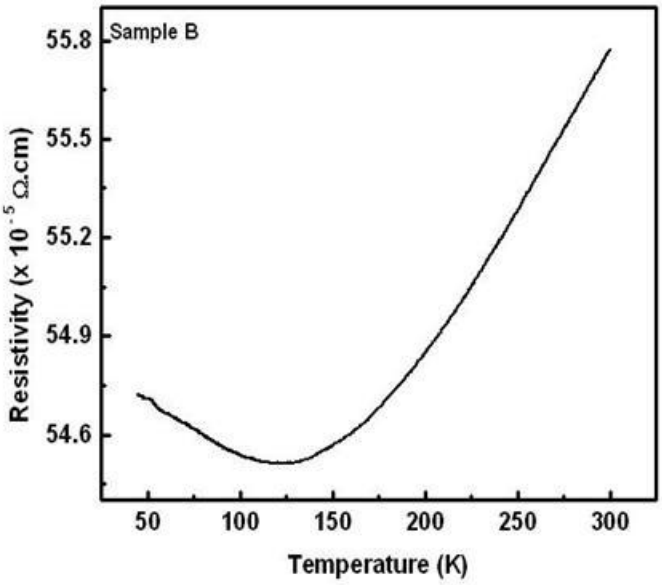

Figure 4.23. Resistivity vs. temperature plots for film grown at 7.5×10^{-5} Torr of oxygen pressure.

For films grown at lower oxygen pressure (Samples A-C), resistivity reaches a minimum at approximately T = 60 K, T = 120 K, and T = 160 K respectively, and consequently exhibit

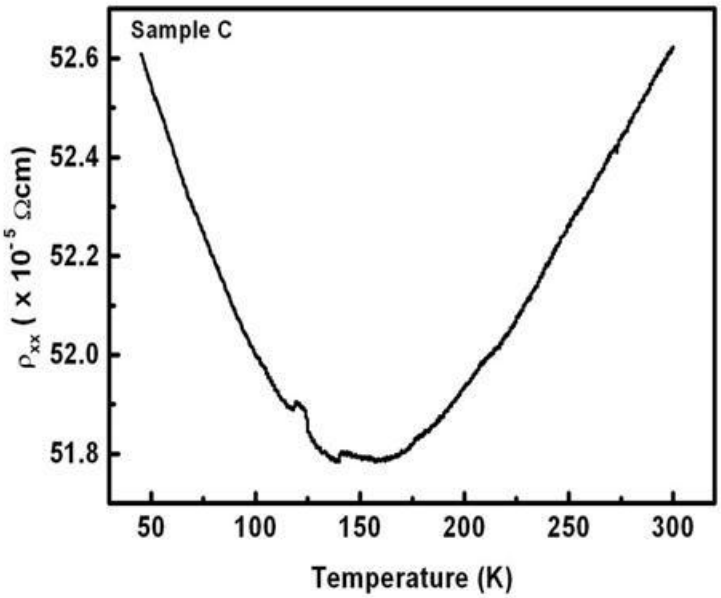

Figure 4.24. Resistivity vs. temperature plots for film grown at 7.5×10^{-4} Torr of oxygen pressure.

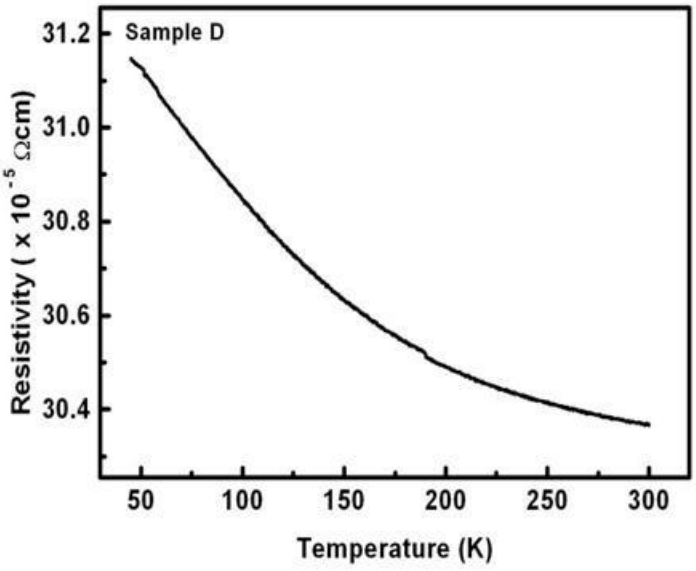

Figure 4.25. Resistivity vs. temperature plots for film grown at 7.5×10^{-3} torr of oxygen pressure.

negative temperature coefficient of resistivity (TCR) below these temperatures. The samples also exhibit metallic behavior and have positive TCR in the temperature ranges 60 < T < 300 K, 120 < T < 300 K, and 160 < T < 300 K respectively. This suggests that two different mechanisms are responsible for electrical dc transport in the two temperature regions. The reason for this behavior is still unclear; however, it has been speculated that the positive TCR could be due to sintering of conducting clusters which form conducting paths through the sample.[36] The observed negative TCR at low temperatures is due to resistivity being dominated by ionized impurity scattering. The negative-to-positive TCR transition temperature in the films was observed to increase with partial oxygen pressure, which indicates that the films become more semiconducting and less metallic as corroborated by the decrease in carrier concentration in Fig. 4.17. Film D, grown at high partial oxygen pressure (sample D) exhibits typical semiconducting behavior with negative TCR in the whole temperature region.

In order to understand the charge transport mechanism in this film, various electrical transport models – hopping conduction and ionized impurity scattering responsible for negative TCR were considered. Hopping conduction is usually denoted by an equation of the form,

$$\rho(T) = B_1 \exp\left[\left(\frac{B_2}{T}\right)^{\frac{1}{q}}\right] \tag{4.9}$$

where B_1, B_2 and q are constants and T is temperature. $q = 1$ characterizes conduction dominated by hopping between localized states distributed in a periodic array (nearest neighbor hopping, NNH); q represents conduction between localized states distributed in a random array (variable range hopping, VRH). For systems characterized by small

metallic grains separated by thin insulating barriers, $q = 2$ is used. In degenerate semiconductors, ionized impurity scattering usually gives rise to negative TCR and the temperature dependence of $\rho(T)$ is given by,

$$\rho(T) \ \alpha \ T^{-3/2} \tag{4.10}$$

From Fig. 4.26, the concave curvature of log $\rho(T)$ vs. $T^{-1/q}$ with $q = 1$, suggests that nearest neighbor hopping (NNH) conduction is not responsible for electrical transport in this sample. Fig. 4.27 as well as the non-linearity of similar log $\rho(T)$ vs. $T^{-1/q}$ plots, for $q = 2$ and $q = 4$ strongly indicate that the transport mechanism is neither governed by localized conduction electrons (hopping) nor scattering of conduction electrons by ionized impurities.

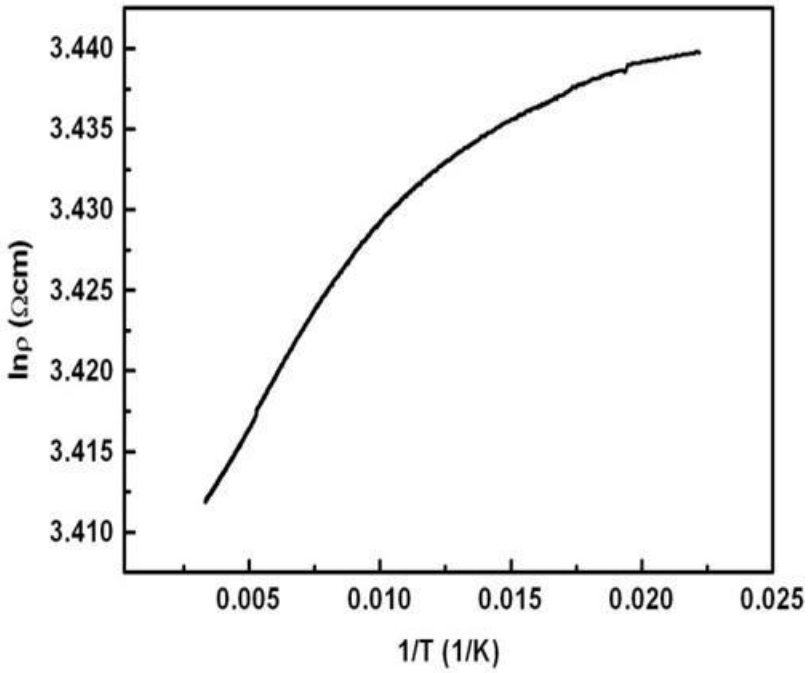

Figure 4.26. ln ρ (T) vs. 1/T for sample D.

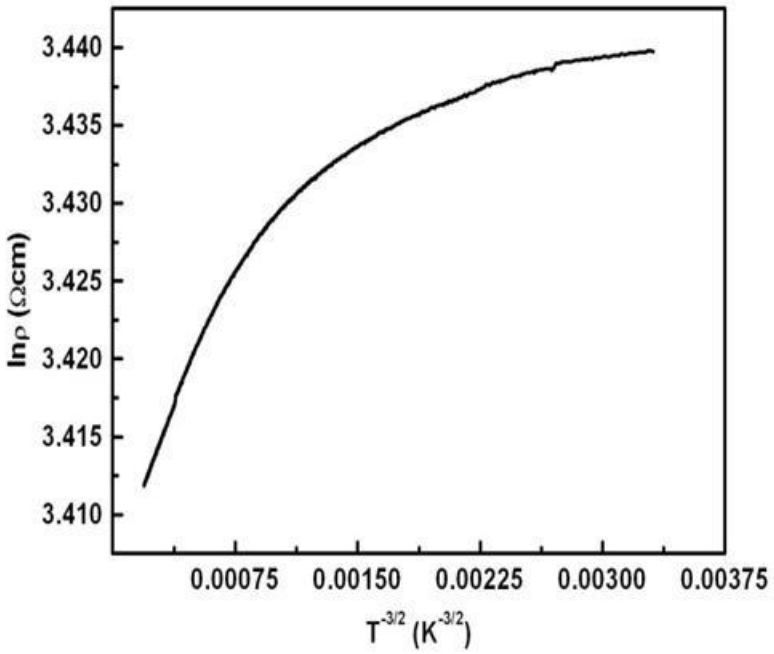

Figure 4.27. ln ρ (T) vs. $T^{-3/2}$ for sample D.

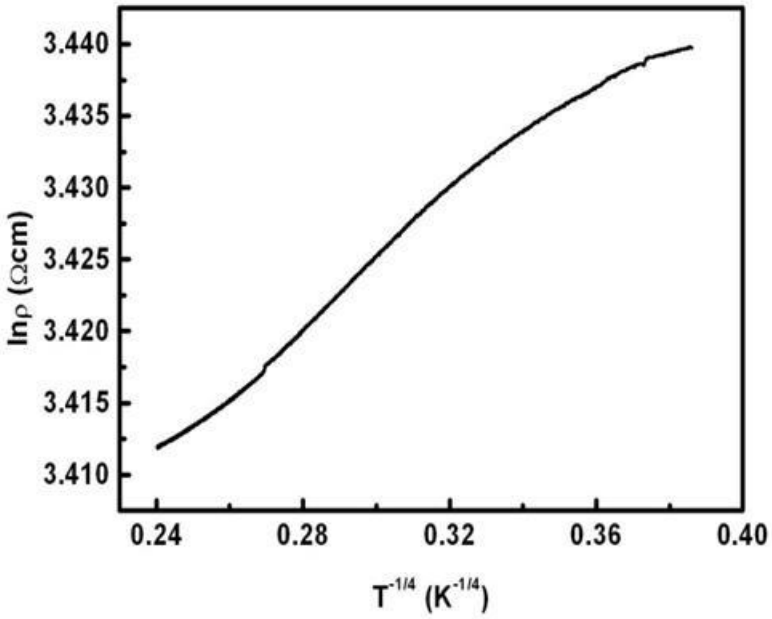

Figure 4.28. ln ρ (T) vs. $T^{-1/4}$ for sample D.

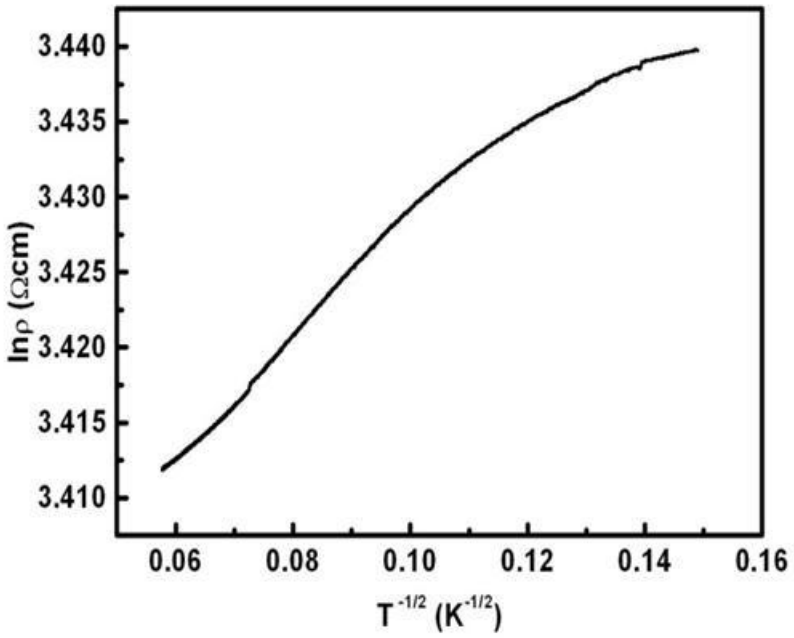

Figure 4.29. ln ρ (T) vs. $T^{-1/2}$ for sample D.

4.4 Magnetic properties

Magnetization (M) vs applied magnetic field (H) data were collected on all the samples using a superconducting quantum interference device (SQUID) magnetometer at various temperatures. M-H data for all the samples show linear behavior at all temperature down to 5 K. Representatives of M-H plots at 300 K are shown in Fig 4.30. The linear behavior of M with H indicates the presence of paramagnetic or antiferromagnetic phase in the films. The non-existence of ferromagnetic ordering in the samples could possibly be due to the presence of Cr clusters which are not usually detectable with x-ray diffraction analysis. The presence of these clusters is usually detectable via high resolution transmission electron microscopy (HRTEM) measurements.

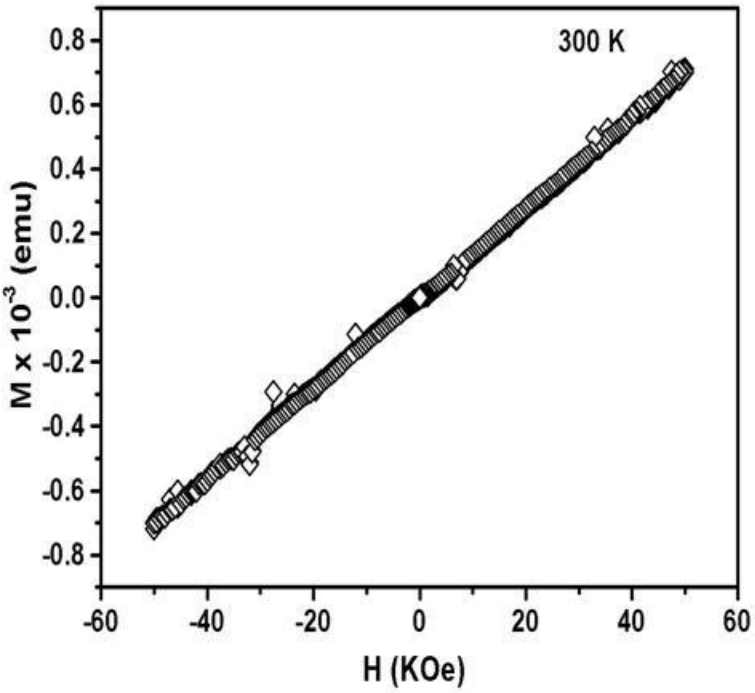

Figure 4.30. Magnetization (M) as a function of magnetic field (H) for sample A.

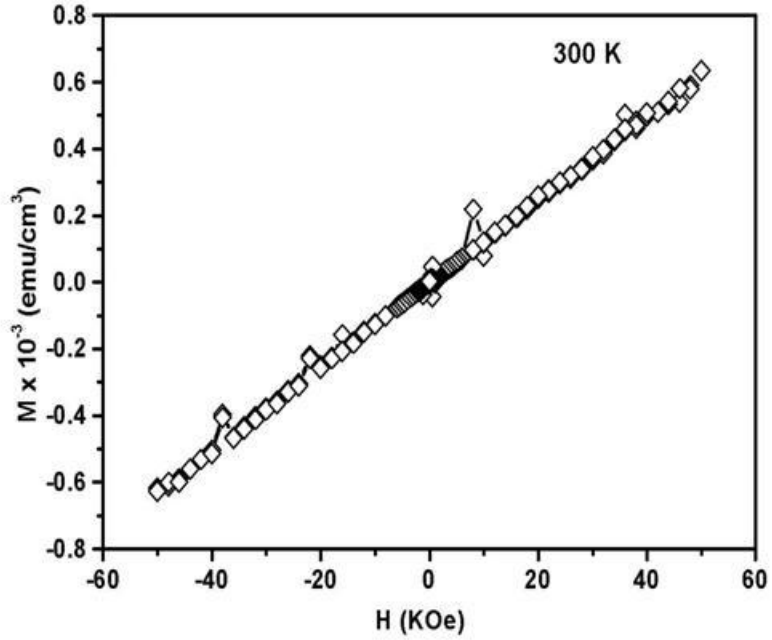

Figure 4.31. Magnetization (M) as a function of magnetic field (H) for sample B.

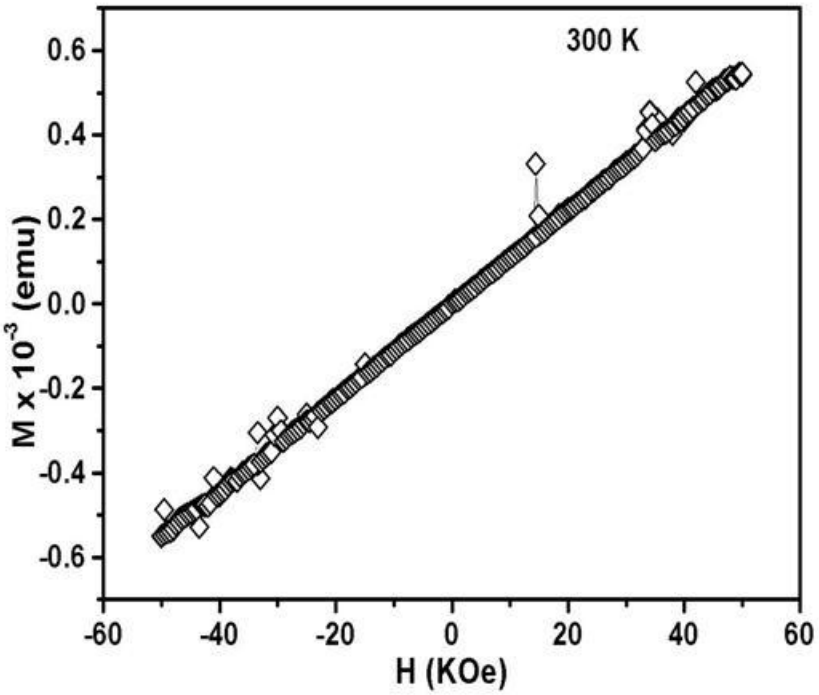

Figure 4.32. Magnetization (M) as a function of magnetic field (H) for sample C.

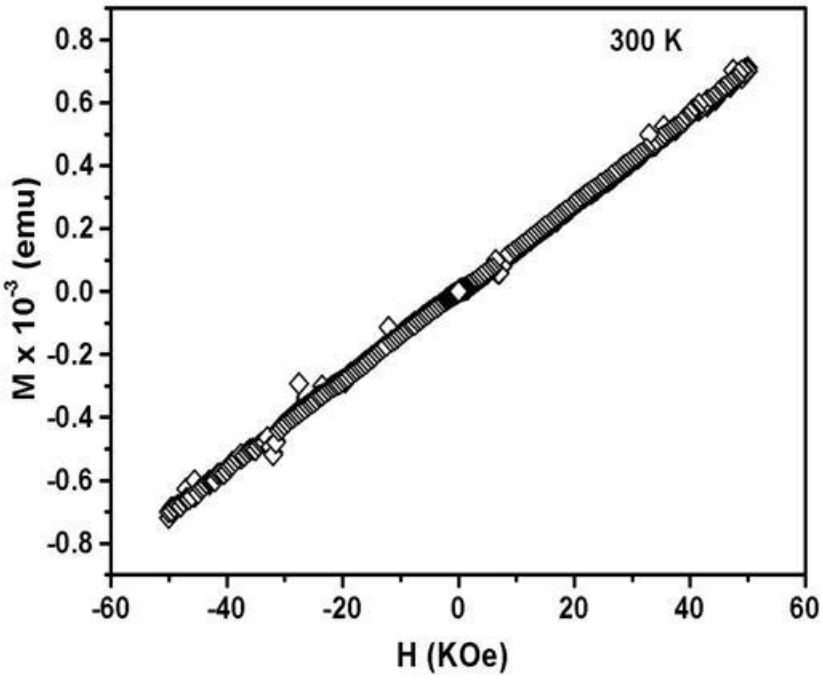

Figure 4.33. Magnetization (M) as a function of magnetic field (H) for sample D.

CHAPTER 5

CONCLUSIONS

The dependence of structural, optical, electrical, magnetic, and magnetotransport properties of chromium doped indium oxide thin films on oxygen vacancies have been investigated. Structural parameters such as lattice constant and particle size, optical properties such transmittance and optical band gap as well as electrical properties are found to be sensitive to oxygen vacancies in the films. However, the magnetic properties of the films are unaffected by oxygen vacancies. Lattice constant and particle size in these films increase with reduction in oxygen vacancies. An increase in the optical transmittance and a reduction in band gap with a decrease in the oxygen vacancies have been observed. The carrier concentration decreases while the carrier mobility increases with decrease in oxygen vacancies. Films with higher oxygen vacancies (Samples A-C) exhibit semiconductor-to-metallic transitions, while film with low oxygen vacancies (Sample D) displayed typical semiconducting behavior. Conventional semiconducting electrical transport in oxide-based (In_2O_3:Cr) DMS films does not follow theory of conventional semiconductors or hopping conduction between localized states. Magnetization measurements carried out on the samples revealed the existence of paramagnetism or antiferromagnetism, and this is possibly due to the Cr segregation. The observed redshift in the optical band gap and increase in carrier mobility brought about by the improvement in crystallinity are traceable to the reduction in oxygen vacancies in the films. In the future, further investigations on control of Cr segregation and electrical and magnetic properties are necessary in order to better understand complex electrical transport and magnetic behavior in oxide-based DMS.

REFERENCES

[1]D. Kumar, J. Antifakos, M. G. Blamire, Z. H. Barber, Appl. Phys. Lett. 84, 5004 (2004).

[2]Zhang, X. Z. Li, B. Xu, D.J. Sellmyer, Appl. Phys. Lett. 86, 212504 (2005).

[3]H. Ohno, H. Munekata, T. Penney, S. von Molnar, L. L. Chang, Phys. Rev. Lett. 68, 2664 (1992).

[4]H. Munekata, H. Ohno, S. von Molnar, Armin Sergmuller, L. L. Chang, S. Esaki, Phys. Rev. Lett. 63, 1849 (1989).

[5]Y. Matsumoto, M. Murakami, T. Shono, T. Hasegawa, T. Fukumara, M. Kawasaki, P. Ahmet, T. Chikyow, S. Koshihara, H. Koinuma, Science 291, 854 (2001).

[6]K. Ueda, H. Tabata, T. Kawai, Appl. Phys. Lett. 79, 988 (2001).

[7]S. B. Ogale, R. J. Choudhury, J. P. Buban, S. E. Lofland, S. R. Shinde, S. N. Kale, V. N Kulkarni, J. Higgins, C. Lanci, J. R. Simpson, N. D. Browning, S. Das Sarma, H. D. Drew, R. L. Greene, T. Venatesan, Phys. Rev. Lett. 91, 077205 (2003).

[8]S. Ramachandran, J. Narayan, J. T. Prater, Appl. Phys. Lett. 88, 242503 (2006).

[9]P.V. Randovanovic, D. R. Gamelin, Phys. Rev. Lett. 91, 157202 (2003).

[10]D. A. Schwartz, D. R. Gamelin, Adv. Mater. 16, 2115 (2004).

[11]N. Y. H. Hong, J. Sakai, A. Hassini, Appl. Phys. Lett. 84, 2602 (2004).

[12]N. H. Hong, W. Prellier, J. Sakai, A. Hassini, Appl. Phys. Lett. 84, 285 (2004).

[13]J. S. Higgins, S. R. Shinde, S. B. Ogale, T. Venkatesan, R. L. Greene, Phys. Rev. B 69, 073201 (2004).

[14]S. B. Ogale, R. J. Choudhury, J. P. Budan, S. E. Lofland, S. R. Shinde, S. N. Kale, V. N. Kulkarni, J. Higgins, C. Lanci, J. R. Simpson, N. D. Browning, S. Das Sarma, H. D. Drew, R. L. Greene, T. Venkatesan, Phys. Rev. Lett. 91, 077205 (2003).

[15]C. B. Fitzgerald, M. Venkatesan, A. P. Douvalis, S. Huber, J. M. D. Coey, T. Bakas, J. Appl. Phys. 95, 7390 (2004).

[16]C. B. Fitzgerald, M. Venkatesan, A. P. Douvalis, S. Huber, J. M. D. Coey, T. Bakas, J. Appl. Phys. 95, 7390 (2004).

[17]N. H. Hong, J. Sakai, N. T. Huong, V. Brize, Appl. Phys. Lett. 87, 102505 (2005).

[18]G. Peleckis, X. Wang, S.X. Dou, Appl. Phys. Lett. 89, 022501 (2006).

[19]J. Philip, A. Punnoose, B. I. Kim, K. M. Reddy, S. Layne, J. O. Holmes, B. Satpati, P. R. Leclair, T. S Santos, J. S. Moodera, Nat. Mater. 5, 298 (2006).

[20]P. Kharel, C. Sudaker, M.B. Sahana, G. Lawes, R. Suryanarayanan, R. Naik, J. Appl. Phys. 101, 09H117 (2007).

[21]R. K. Gupta, K. Ghosh, S. R. Mishra, P. K. Kahol, Appl. Surf. Sci. 253, 9422 (2007).

[22]Han-Chang Pan, Ming-Hua Shiao, Chien-Ying Su, Chien-Nan Hsiao, J. Vac. Sci. Technol. A 23, 1187 (2005).

[23]E. M. Conwell, Phys. Rev. 103, 51 (1956).

[24]A. Miller, E. Abrahams, Phys. Rev. 120, 745 (1960).

[25]N. Mott, Metal-Insulator Transitions (Taylor and Francis, London, 1990).

[26]P. Sheng, Phys. Rev. B 21, 2180 (1980).

[27]C. Zener, Phys. Rev. 81, 440 (1951).

[28]A. H. Macdonald, P. Schiffer, N. Samarth, Nat. Mater. 4, 195 (2005).

[29]J. M. D. Coey, M. Venkatesan, C. B. Fitzegerald, Nat. Mater. 4, 298 (2005).

[30]D. J. Piour, Jn, S. Das Sarma, Phys. Rev. Lett. 97, 127201 (2006).

[31]S. Tsunekawa, K. Ishikawa, Z.-Q. Li, Y. Kawazoe, A. Kasuya, Phys. Rev. Lett. 85, 3440 (2000).

[32]X.-D. Zhou, W. Hueber, Appl. Phys. Lett. 79, 3512 (2001).

[33]J. Hamberg, C. G. Granqvist, J. Appl. Phys. 60, R123 (1986).

[34]S. T. Tan, B. J. Chen, X. W. Sun, W. J. Fan, H. S Kwok, X. H. Zhang, S. J. Chua, J. Appl. Phys. 98, 013505 (2005).

[35]N. Lebedeva, S. Novikov, T. Saloniemi, and P. Kuivalainen, Pysica Scripta Vol. T114 85 (2004).

[36]J. Ederth, P. Johnsson, G. A. Niklasson, A. Hoel, A. Hultaker, P. Hexsler, C. G. Granqvist, A. R. van Doom, M. J. Jongerius, D. Burgard, Phys. Rev. B 68, 155410 (2003).